

# A data-analysis driven comparison of analytic and numerical coalescing binary waveforms: nonspinning case

Yi Pan,<sup>1</sup> Alessandra Buonanno,<sup>1</sup> John G. Baker,<sup>2</sup> Joan Centrella,<sup>2</sup> Bernard J. Kelly,<sup>2</sup> Sean T. McWilliams,<sup>1</sup> Frans Pretorius,<sup>3</sup> and James R. van Meter<sup>2,4</sup>

<sup>1</sup>*Department of Physics, University of Maryland, College Park, MD 20742*

<sup>2</sup>*Gravitational Astrophysics Laboratory, NASA Goddard Space Flight Center, 8800 Greenbelt Rd., Greenbelt, MD 20771*

<sup>3</sup>*Department of Physics, Princeton University, Princeton, NJ 08544*

<sup>4</sup>*Center for Space Science & Technology, University of Maryland Baltimore County, Physics Department, 1000 Hilltop Circle, Baltimore, MD 21250*

(Dated: October 22, 2018)

We compare waveforms obtained by numerically evolving nonspinning binary black holes to post-Newtonian (PN) template families currently used in the search for gravitational waves by ground-based detectors. We find that the time-domain 3.5PN template family, which includes the inspiral phase, has fitting factors (FFs)  $\geq 0.96$  for binary systems with total mass  $M = 10\text{--}20M_\odot$ . The time-domain 3.5PN effective-one-body template family, which includes the inspiral, merger and ring-down phases, gives satisfactory signal-matching performance with FFs  $\geq 0.96$  for binary systems with total mass  $M = 10\text{--}120M_\odot$ . If we introduce a cutoff frequency properly adjusted to the final black-hole ring-down frequency, we find that the frequency-domain stationary-phase-approximated template family at 3.5PN order has FFs  $\geq 0.96$  for binary systems with total mass  $M = 10\text{--}20M_\odot$ . However, to obtain high matching performances for larger binary masses, we need to either extend this family to unphysical regions of the parameter space or introduce a 4PN order coefficient in the frequency-domain GW phase. Finally, we find that the phenomenological Buonanno-Chen-Vallisneri family has FFs  $\geq 0.97$  with total mass  $M = 10\text{--}120M_\odot$ . The main analyses use the noise spectral-density of LIGO, but several tests are extended to VIRGO and advanced LIGO noise-spectral densities.

PACS numbers: 04.25.Dm, 04.30.Db, 04.70.Bw, x04.25.Nx, 04.30.-w, 04.80.Nn, 95.55.Ym

## I. INTRODUCTION

The search for gravitational-waves (GWs) from coalescing binary systems with laser interferometer GW detectors [1, 2, 3, 4, 5] is based on the matched-filtering technique, which requires accurate knowledge of the waveform of the incoming signal. In the last couple of years there have been several breakthroughs in numerical relativity (NR) [6, 7, 8], and now independent groups are able to simulate the inspiral, merger and ring-down phases of generic black-hole (BH) merger scenarios, including different spin orientations and mass ratios [9]. However, the high computational cost of running such simulations makes it difficult to generate sufficiently long inspiral waveforms that cover the parameter space of astrophysical interest.

References [10, 11] found good agreement between analytic (based on the post-Newtonian (PN) expansion) and numerical waveforms emitted during the inspiral, merger and ring-down phases of equal-mass, nonspinning binary BHs. Notably, the best agreement is obtained with 3PN or 3.5PN adiabatic waveforms [12] (henceforth denoted as Taylor PN waveforms) and 3.5PN effective-one-body (EOB) waveforms [13, 14, 15, 16, 17, 18, 19]. In addition to the inspiral phase the latter waveforms include the merger and ring-down phases. Those comparisons suggested that it should be possible to design hybrid numerical/analytic templates, or even purely analytic templates with the full numerics used to guide the patching together of the inspiral and ring-down waveforms. This is

an important avenue to template construction as eventually thousands of waveform templates may be needed to extract the signal from the noise, an impossible demand for NR alone. Once available, those templates could be used by ground-based laser interferometer GW detectors, such as LIGO, VIRGO, GEO and TAMA, and in the future by the laser interferometer space antenna (LISA) for detecting GWs emitted by solar mass and supermassive binary BHs, respectively.

This paper presents a first attempt at investigating the closeness of the template families currently used in GW inspiral searches to waveforms generated by NR simulations. Based on this investigation, we shall propose adjustments to the templates so that they include merger and ring-down phases. In contrast, Ref. [21] examined the use of numerical waveforms in inspiral searches, and compared numerical waveforms to the ring-down templates currently used in burst searches. Similar to the methodology presented here, fitting factors (FFs) [see Eq. (2) below] are used in Ref. [21] to quantify the accuracy of numerical waveforms for the purpose of detection, as well as the overlap of burst templates with the waveforms. Reference [21] found that by computing FFs between numerical waveforms from different resolution simulations of a given event, one can recast the numerical error as a maximum FF that the numerical waveform can resolve. In other words, any other template or putative signal convolved with the highest resolution numerical simulation that gives a FF equal to or larger than this maximum FF is, for the purpose of de-

tection, indistinguishable from the numerical waveform. We will explore this aspect of the problem briefly. The primary conclusions we will draw from the analysis do not crucially depend on the exactness of the numerical waveforms. What counts here is that the templates can capture the dominant spectral characteristics of the true waveform.

For our analysis we shall focus on two nonspinning equal-mass binary simulation waveforms which differ in length, initial conditions, and the evolution codes used to compute them: Cook-Pfeiffer quasi-equilibrium initial data built on Refs. [22, 23, 24, 25, 26] evolved with Pretorius' generalized harmonic code [6], and Brandt-Brügmann puncture data [27] evolved using the Goddard group's moving-puncture code [8]. We also consider two nonspinning unequal-mass binary simulations with mass ratios  $m_2/m_1 = 1.5$  and  $m_2/m_1 = 2$  produced by the Goddard group.

The paper is organized as follows. In Sec. II we discuss the phase differences between PN inspiraling templates. In Sec. III we build *hybrid* waveforms by stitching together PN and NR waveforms. We try to understand how many NR cycles are needed to obtain good agreement between NR and PN waveforms, to offer a guide for how long PN waveforms can be used as accurate templates. In Sec. IV we compute the FFs between several PN template families and NR waveforms. We first focus on low-mass binary systems with total mass  $M = 10\text{--}30M_\odot$ , then high-mass binary systems with total mass  $M = 30\text{--}120M_\odot$ . Finally, Sec. V contains our main conclusions. In Appendix A we comment on how different representations of the energy-balance equations give GW frequencies closer to or farther from the NR ones.

## II. PHASE DIFFERENCES IN POST-NEWTONIAN INSPIRALING MODELS

Starting from Ref. [28], which pointed out the importance of predicting GW phasing with the highest possible accuracy when building GW templates, many subsequent studies [14, 18, 19, 20, 29, 31, 32, 33] (those references are restricted to the nonspinning case) focused on this issue and thoroughly tested the accuracy of those templates, proposing improved representations of them. These questions were motivated by the observation that comparable-mass binary systems with total mass higher than  $30M_\odot$  merge in-band with the highest signal-to-noise ratio (SNR) for LIGO detectors. It follows that the corresponding templates demand an improved analysis.

In the absence of NR results and under the urgency of providing templates to search for comparable-mass binary BHs, the analytic PN community pushed PN calculations to higher PN orders, notably 3.5PN order [12], and also proposed ways of resumming the PN expansion, either for conservative dynamics (the EOB approach [13, 16, 17]), radiation-reaction effects (the Padé

resummation [19]), or both [14, 18]. Those results lead to several conclusions: (i) 3PN terms improve the comparison between analytic and (numerical) quasi-equilibrium predictions [23, 26, 34, 35]; (ii) Taylor expanded and resummed PN predictions for equal-mass binary systems are much closer at 3.5PN order than at previous PN orders, indicating a convergence between the different schemes [18, 20, 31]; (iii) the two-body motion is quasi-circular until the end of a rather blurred plunge [14], (iv) the transition to ring-down can be described by an extremely short merger phase [14, 18]. Today, with the NR results we are in a position to sharpen the above conclusions, and to start to assess the closeness of analytic templates to numerical waveforms.

Henceforth, we restrict the analysis to the three time-domain physical template families which are closest to NR results [10, 11]: the adiabatic Taylor PN model (Tpn) [see, e.g., Eqs. (1), (10), and (11)–(13) in Ref. [30]] computed at 3PN and 3.5PN order, and the nonadiabatic EOB model (Epn) [see e.g., Eqs. (3.41)–(3.44) in Ref. [14]] computed at 3.5 PN order. We shall denote our models as Tpn(n) and Epn(n), n being the PN order. The Tpn model is obtained by solving a particular representation of the balance equation. In Appendix A we briefly discuss how time-domain PN models based on different representations of the energy-balance equation would compare with NR results.

The waveforms we use are always derived in the so-called *restricted approximation* which uses the amplitude at Newtonian order and the phase at the highest PN order available. They are computed by solving PN dynamical equations providing the instantaneous frequency  $\omega(t)$  and phase  $\phi(t) = \phi_0 + \int_{t_0}^t \omega(t')dt'$ , thus

$$h(t) = \mathcal{A}\omega(t)^{2/3} \cos[2\phi(t)], \quad (1)$$

where  $t_0$  and  $\phi_0$  are the initial time and phase, respectively, and  $\mathcal{A}$  is a constant amplitude, irrelevant to our discussion. The inclusion of higher-order PN corrections to the amplitude can be rather important for certain unequal-mass binary systems, and will be the subject of a future study.

When measuring the differences between waveforms we weight them by the power spectral-density (PSDs) of the detector, and compute the widely used *fitting factor* (FF) (i.e., the ambiguity function or normalized overlap), or equivalently the *mismatch* defined as 1-FF. Following the standard formalism of matched-filtering [see, e.g., Refs. [19, 31, 36]], we define the FF as the overlap  $\langle h_1(t), h_2(t) \rangle$  between the waveforms  $h_1(t)$  and  $h_2(t)$ :

$$\begin{aligned} \langle h_1(t), h_2(t) \rangle &\equiv 4 \operatorname{Re} \int_0^\infty \frac{\tilde{h}_1(f) \tilde{h}_2^*(f)}{S_h(f)} df, \\ \text{FF} &\equiv \max_{t_0, \phi_0, \lambda^i} \frac{\langle h_1, h_2(t_0, \phi_0, \lambda^i) \rangle}{\sqrt{\langle h_1, h_1 \rangle \langle h_2(t_0, \phi_0, \lambda^i), h_2(t_0, \phi_0, \lambda^i) \rangle}}, \end{aligned} \quad (2)$$

where  $\tilde{h}_i(f)$  is the Fourier transform of  $h_i(t)$ , and  $S_h(f)$  is the detector's PSD. Thus, the FF is the normalized

overlap between a target waveform  $h_1(t)$  and a set of template waveforms  $h_2(t_0, \phi_0, \lambda^i)$  maximized over the initial time  $t_0$ , initial phase  $\phi_0$ , and other parameters  $\lambda^i$ . Sometimes we are interested in FFs that are optimized *only* over  $t_0$  and  $\phi_0$ ; we shall denote these as  $\text{FF}_0$ . For data-analysis purposes, the FF has more direct meaning than the phase evolution of the waveforms, since it takes into account the PSDs and is proportional to the SNR of the filtered signal. Since the event rate is proportional to the cube of the SNR, and thus to the cube of the FF, a  $\text{FF} = 0.97$  corresponds to a loss of event rates of  $\sim 10\%$ . A template waveform is considered a satisfactory representation of the target waveform when the FF is larger than 0.97.

When comparing two families of waveforms, the FF is optimized over the initial phase of the template waveform, and we also need to specify the initial phase of the target waveform. Since there is no preferred initial phase of the target, two options are usually adopted: (i) the initial phase *maximizes* the FF or (ii) it *minimizes* the FF. The resulting FFs are referred to as the *best* and *minimax* FFs [29]. All FFs we present in this paper are minimax FFs. Although the FF of two waveform families is generally asymmetric under interchange of the template family [31], the best and the minimax  $\text{FF}_0$ s are symmetric (see Appendix B of Ref. [29] for details). Henceforth, when comparing two waveform families using  $\text{FF}_0$ , we do not need to specify which family is the target.

We shall consider three interferometric GW detectors: LIGO, advanced LIGO and VIRGO. The latter two have better low-frequency sensitivity and broader bandwidth. For LIGO, we use the analytic fit to the LIGO design PSD given in Ref. [20]; for advanced LIGO we use the broadband configuration PSD given in Ref. [37]; for VIRGO we use the PSD given in Ref. [20].

In Fig. 1, we show the  $\text{FF}_0$ s as functions of the accumulated difference in the number of GW cycles between waveforms generated with different inspiraling PN models and for binary systems with different component masses. We first generate two waveforms by evolving two PN models, say, “PN<sub>1</sub>” and “PN<sub>2</sub>” which start at the same GW frequency  $f_{\text{GW}} = 30\text{Hz}$  and have the same initial phase. The two waveforms are terminated at the same ending frequency  $f_{\text{GW}} = f_{\text{end}}$  up to a maximum  $f_{\text{end,max}} = \min(f_{\text{end,PN}_1}, f_{\text{end,PN}_2})$ , where  $f_{\text{end,PN}}$  is the frequency at which the PN inspiraling model ends. (For Tpn models this is the frequency at which the PN energy has a minimum; for Epn models it is the EOB light-ring frequency.) Then, we compute the difference in phase and number of GW cycles accumulated until the ending frequency

$$\Delta N_{\text{GW}} = \frac{\Delta\phi}{\pi} = \frac{1}{\pi} [\phi_{\text{PN}_1}(f_{\text{end}}) - \phi_{\text{PN}_2}(f_{\text{end}})]. \quad (3)$$

By varying  $f_{\text{end}}$  (up to  $f_{\text{end,max}}$ )  $\Delta N_{\text{GW}}$  changes, though not necessarily monotonically. Although there seems to be a loose correlation between the  $\text{FF}_0$ s and  $\Delta N_{\text{GW}}$ , it is hard to quantify it as a one-to-one correspondence.

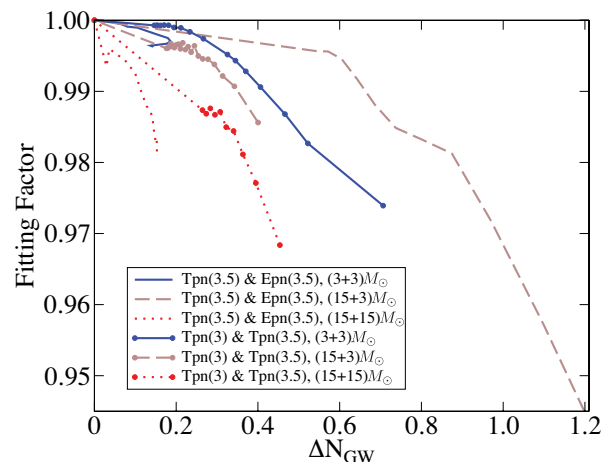


FIG. 1: We show  $\text{FF}_0$ s between waveforms generated from the three PN models Tpn(3), Tpn(3.5) and Epn(3.5) versus  $\Delta N_{\text{GW}}$  [see Eq. (3)]. The  $\text{FF}_0$ s are evaluated with LIGO’s PSD. Note that for Tpn(3.5) and Epn(3.5) and a  $(15+3)M_\odot$  binary, the lowest  $\text{FF}_0$  is 0.78 and the difference in the number of GW cycles  $\Delta N_{\text{GW}} \simeq 2$ . In the limit  $\Delta N_{\text{GW}} \rightarrow 0$ , the  $\text{FF}_0$  goes to unity.

For example, a phase difference of about half a GW cycle ( $\Delta N_{\text{GW}} \simeq 0.5$ ) is usually thought to be significant. However, here we find relatively high  $\text{FF}_0$ s between 0.97 and  $> 0.99$ , depending on the masses of the binary and the specific PN model used. This happens because the FF between two waveforms is not determined by the total phase difference accumulated, but rather by how the phase difference accumulates across the detector’s most sensitive frequency band. The relation between FFs and phase differences is also blurred by the maximization over the initial time and phase: shifting the phase by half a cycle from the most sensitive band to a less sensitive band can increase the matching significantly. We conclude that with LIGO’s PSD, after maximizing *only* on initial phase and time, Epn(3.5) and Tpn(3.5) templates are close to each other for comparable-mass binary systems  $M = 6\text{--}30M_\odot$  with  $\text{FF}_0 \gtrsim 0.97$ , but they can be different for mass ratios  $m_2/m_1 \simeq 0.3$  with  $\text{FF}_0$  as low as  $\simeq 0.8$ . Tpn(3) and Tpn(3.5) templates have  $\text{FF}_0 \gtrsim 0.97$  for the binary masses considered. Note that for  $m_2/m_1 = 1$  [ $\simeq 0.3$ ] binary systems, Tpn(3.5) is closer to Epn(3.5) [Tpn(3)] than to Tpn(3) [Epn(3.5)]. Note also that when maximizing on binary masses the FFs can increase significantly, for instance, for a  $(15+3)M_\odot$  binary, the FF between Tpn(3.5) and Epn(3.5) waveforms becomes  $> 0.995$ , whereas  $\text{FF}_0 \simeq 0.8$ .

### III. BUILDING AND COMPARING HYBRID WAVEFORMS

Recent comparisons [10, 11] between analytic and numerical inspiraling waveforms of nonspinning, equal-mass

binary systems have shown that numerical waveforms are in good agreement with Epn(3.5), Tpn(3) and Tpn(3.5) waveforms. Those results were assessed using eight and sixteen numerical inspiral GW cycles. Can we conclude from these analyses that Epn(3.5), Tpn(3.5) and Tpn(3) can safely be used to build a template bank for detecting *inspiraling* GW signals? A way to address this question is to compute the mismatch between hybrid waveforms built by attaching either Epn or Tpn waveforms to the *same* numerical waveform, and varying the time when the attachment is made. This is equivalent to varying the number of numerical GW cycles  $n$  in the hybrid template. The larger  $n$  the smaller the mismatch, as we are using the same numerical segment in both waveforms. For a desired maximum mismatch, say 3%, we can then find the smallest number  $n$  of numerical cycles that is required in the hybrid waveform. This number will, of course, depend on the binary mass and the PSD of each detector.

### A. Hybrid waveforms

We build hybrid waveforms by connecting PN waveforms to NR waveforms at a chosen point in the late inspiral stage. As mentioned before, we use NR waveforms generated with Pretorius' [10] code and the Goddard group's [38] code. Pretorius' waveform is from an equal-mass binary with total mass  $M$ , and equal, corotating spins ( $a = 0.06$ ). The simulation lasts  $\simeq 671M$ , and the waveform has  $\simeq 8$  cycles before the formation of the common apparent horizon. The Goddard waveform refers to an equal-mass nonspinning binary. The simulation lasts about  $\simeq 1516M$ , and the waveform has  $\simeq 16$  cycles before merger.

Since we will present results from these two waveforms it is useful to first compare them by computing the  $FF_0$ . Although the binary parameters considered by Pretorius and Goddard are slightly different, we expect the waveforms, especially around the merger stage, to be fairly close. Comparisons between (shorter) waveforms computed with moving punctures and generalized-harmonic gauge were reported in Ref. [39], where the authors discussed the different initial conditions, wave extraction techniques, and compared the phase, amplitude and frequency evolutions. Since the two simulations use different initial conditions and last for different amounts of time we cut the longer Goddard waveform at roughly the frequency where the Pretorius waveform starts. In this way we compare waveforms that have the same length between the initial time and the time at which the wave amplitude reaches its maximum. In Fig. 2, we show the  $FF_0$  as function of the total binary mass. Despite differences in the two simulations the  $FF_0$ s are rather high. The waveforms differ more significantly at lower frequencies. Indeed, as the total mass decreases the  $FF_0$ s also decrease as these early parts of the waveform contribute more to the signal power given LIGO's PSD.

Any waveform extracted from a numerical simulation will inherit truncation errors, affecting both the waveform's amplitude and phase [10, 21, 38]. To check whether those differences would change the results of the comparisons between NR and PN waveforms, we plot in Fig. 2 the  $FF_0$ s versus total binary mass between two Goddard waveforms generated from a high and a medium resolution run [38]. The  $FF_0$ s are extremely high ( $> 0.995$ ).

Based on the comparisons between high and medium resolution waveforms, we can estimate the FFs between high resolution and exact waveforms. If we have several simulations with different resolutions, specified by the mesh-spacings  $x_i$ , and  $x_i$  are sufficiently small, we can assume that the waveforms  $h_i$  are given by

$$h_i = h_0 + x_i^n h_d, \quad (4)$$

where  $n$  is the convergence factor of the waveform,  $h_0$  is the exact waveform generated from the infinite resolution run ( $x_0 \rightarrow 0$ ), and  $h_d$  is the leading order truncation error contribution to the waveform and is independent of the mesh spacing  $x_i$ . We find that the mismatch between the waveforms  $h_i$  and  $h_j$ ,  $1 - FF_{ij}$ , scales as

$$1 - FF_{ij} \propto (x_i^n - x_j^n)^2. \quad (5)$$

In the Goddard simulations, the high and medium resolution runs have mesh-spacing ratio  $x_h/x_m = 5/6$ , and the waveform convergence rate is  $n = 4$  [38]. The FF between the high resolution and exact waveforms  $h_h$  and  $h_0$  is given by

$$FF_{0h} = 1 - 0.87(1 - FF_{hm}), \quad (6)$$

where  $FF_{hm}$  is the FF between the high and medium resolution waveforms  $h_h$  and  $h_m$ . That is to say, the mismatch between  $h_h$  and  $h_0$  is slightly smaller than that between  $h_h$  and  $h_m$ , where the latter can be derived from the FFs shown in Fig. 2. Henceforth, we shall always use high-resolution waveforms. A similar calculation for Pretorius' waveform gives  $FF_{0h} = 1 - 0.64(1 - FF_{hm})$ , though here  $x_h/x_m = 2/3$  and  $n = 2$ . See Fig. 6 of Ref. [21] for a plot of  $FF_{hm}$  calculated from the evolution of the Cook-Pfeiffer initial data <sup>1</sup>; there  $FF_0$  ranges from  $\approx 0.97$  for  $M/M_s = 30$  to  $\approx 0.99$  for  $M/M_s = 100$ . In other words, the mismatch between Goddard's and Pretorius' waveform shown in Fig.2 is less than the estimated mismatch from numerical error in the latter waveform.

We build hybrid waveforms by stitching together the PN and NR waveforms computed for binary systems with the *same* parameters. At the point where we connect the

<sup>1</sup> The plot in Ref. [21] is for "d=16" corotating Cook-Pfeiffer initial data, whereas the results presented here are from "d=19" initial data. However, the resolutions used for both sets were the same, and thus the mismatches should be similar, in particular in the higher mass range.



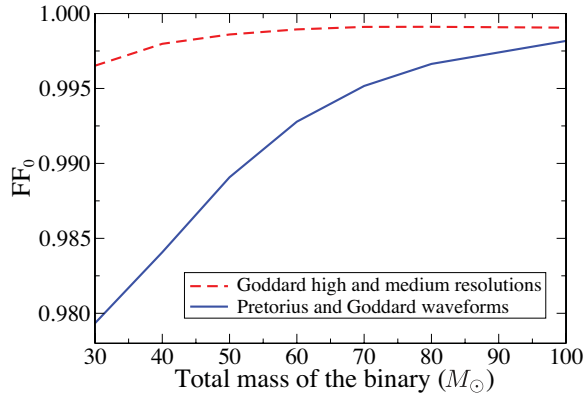


FIG. 2:  $FF_0$  between NR waveforms as a function of the binary total-mass  $M$ . The solid curve are generated for waveforms from Pretorius and the Goddard group. The longer Goddard waveform is shortened such that both waveforms last  $\simeq 671M$  and contain  $\simeq 8$  cycles. The dashed curve is generated for waveforms from the high-resolution and medium resolution simulations of the Goddard group. All FFs are evaluated using LIGO's PSD.

two waveforms, we tune the initial time  $t_0$  so that the frequency of the PN waveform is almost the same as the frequency of the NR waveform (there is a subtlety trying to match exactly the frequencies that is discussed at the end of this section). The initial phase  $\phi_0$  is then chosen so that the strain of the hybrid waveform is continuous at the connecting point.

In Fig. 3, we show two examples of hybrid waveforms of an equal-mass binary. We stitch the waveforms at points where effects due to the initial-data transient pulse are negligible. We find an amplitude difference on the order of  $\sim 10\%$  between the Goddard waveform and the restricted PN waveform. This difference is also present in Pretorius' waveform, but it is somewhat compensated for by amplitude modulations caused by eccentricity in the initial data. In Ref. [38] it was shown that PN waveforms with 2.5PN amplitude corrections give better agreement (see e.g., Fig. 12 in Ref. [38]). However, the maximum amplitude errors in the waveforms are also on the order of 10% [10, 38]. Since neither 2PN nor other lower PN order corrections to the amplitudes are closer to the 2.5PN order, we cannot conclude that 2.5PN amplitude corrections best approximate the numerical waves. Thus, we decide to use two sets of hybrid waveforms: one constructed with restricted PN waveforms, and the other with restricted PN waveforms rescaled by a single amplitude factor, which eliminates amplitude differences with the NR waveforms. We shall see that the difference between these two cases is small for the purpose of our tests.

The amplitude difference between PN and NR waveforms is computed at the same connecting-point GW fre-

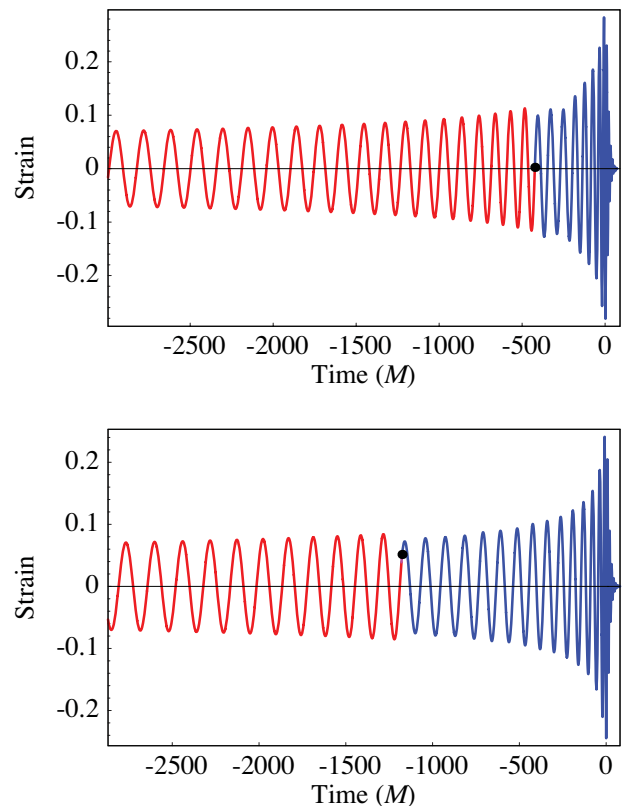


FIG. 3: We show two examples of hybrid waveforms, starting from 40Hz. The PN waveforms are generated with the Tpn(3.5) model, and the NR waveforms in the upper and lower panels are generated from Pretorius' and Goddard's simulations, respectively. We mark with a dot the point where we connect the PN and NR waveforms.

quency. There is another effect which causes a jump in the hybrid-waveform amplitude. This is a small frequency difference between PN and NR waveforms at the connecting point. All our NR waveforms contain small eccentricities [10, 38]. As a consequence, the frequency evolution  $\omega(t)$  oscillates. To reduce this effect we follow what is done in Ref. [38] and fit the frequency to a monotonic quartic function. When building the hybrid waveform, we adjust the PN frequency to match the quartic fitted frequency (instead of the oscillatory, numerical frequency) at the connecting point. Since the restricted PN amplitude is proportional to  $\omega^{2/3}(t)$  [see Eq. (1)], this slight difference between  $\omega$ s at the connecting point creates another difference between the NR and PN amplitudes. Nevertheless, this difference is usually smaller (for Goddard's waveform) or comparable (for Pretorius') to the amplitude difference discussed above.

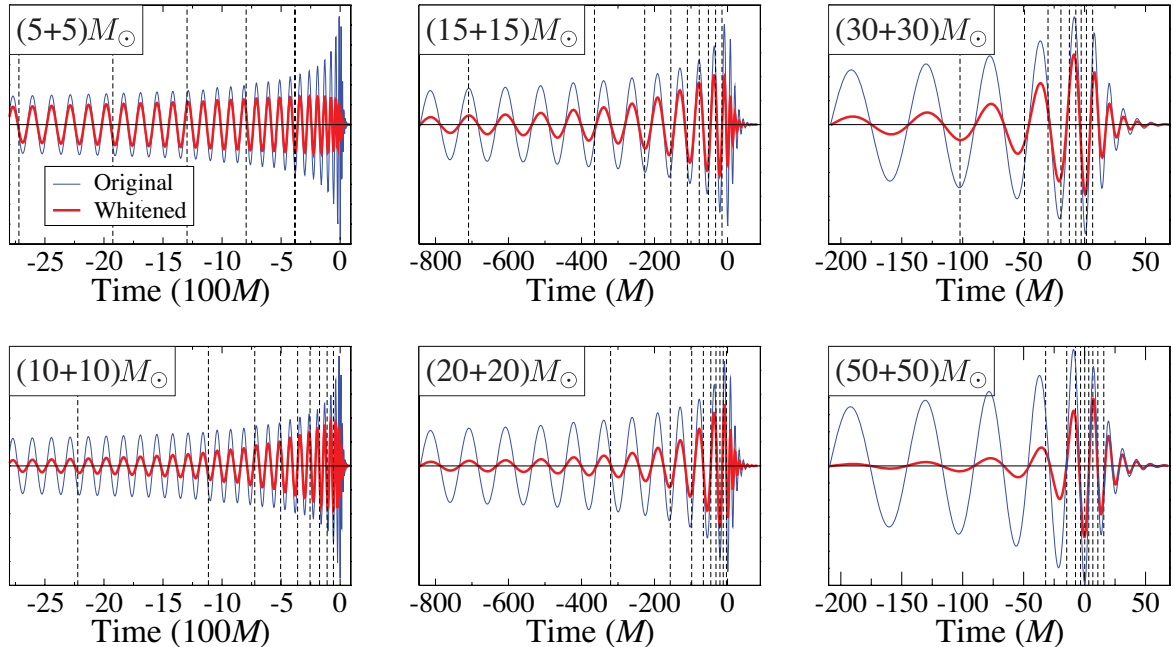


FIG. 4: Distribution of GW signal power. In each panel, we plot a hybrid waveform (a Tpn waveform stitched to the Goddard waveform) in both its original form (blue curve) and its “whitened” form (red curve) [44]. We show waveforms from six binary systems with total masses  $10M_\odot$ ,  $20M_\odot$ ,  $30M_\odot$ ,  $40M_\odot$ ,  $60M_\odot$  and  $100M_\odot$ . The vertical lines divide the waveforms into segments, where each segment contributes 10% of the total signal power.

### B. Distribution of signal power in gravitational waveforms

To better understand the results of the FFs between hybrid waveforms, we want to compute how many *significant* GW cycles are in the LIGO frequency band. By significant GW cycles we mean the cycles that contribute most to the signal power, or to the SNR of the filtered signal. Since GW frequencies are scaled by the total binary mass, the answer to this question depends on both the PSD and the total mass of a binary.

In Fig. 4, we show the effect of the LIGO PSD on the distribution of signal power for several waves emitted by coalescing binary systems with different total masses. In each panel, we plot a hybrid waveform (a Tpn waveform stitched to the Goddard waveform) in both its original form and its “whitened” form [44]. The whitened waveform is generated by Fourier-transforming the original waveform into the frequency domain, rescaling it by a factor of  $1/\sqrt{S_h(f)}$ , and then inverse-Fourier-transforming it back to the time domain. The reference time  $t = 0$  is the peak in the amplitude of the unwhitened waveform. The amplitude of a segment of the whitened waveform indicates the relative contribution of that segment to the signal power and takes into account LIGO’s PSD. Both waveforms are plotted with arbitrary amplitudes, and the unwhitened one always has the larger amplitude. The absolute amplitude of a waveform, or equivalently the

distance of the binary, is not relevant in these figures unless the redshift  $z$  becomes significant. In this case the mass of the binary is the redshifted mass  $(1+z)M$ . Vertical lines in each figure divide a waveform into segments, where each segment contributes 10% of the total signal power. In each plot, except for the  $10M_\odot$ -binary one, we show all 9 vertical lines that divide the waveforms into 10 segments. In the  $10M_\odot$ -binary plot we omit the early part of the inspiral phase that accounts for 50% of the signal power, as it would be too long to show.

The absolute time-scale of a waveform increases linearly with total mass  $M$ ; equivalently the waveform is shifted toward lower frequency bands. For a  $M = 10M_\odot$  binary, the long inspiral stage generates GWs with frequencies spanning the most sensitive part of the LIGO band, around 150Hz, while for an  $M = 100M_\odot$  binary, only the merger signal contributes in this band. Thus, for low-mass binary systems, most of the contribution to the signal power comes from the long inspiral stage of the waveform, while for high-mass binary systems most of the contribution comes from the late inspiral, merger, and ring-down stages. Understanding quantitatively the distribution of signal power will let us deduce how many, and which, GW cycles are significant for the purpose of data analysis. We need accurate waveforms from either PN models or NR simulations for at least those significant cycles.

From Fig. 4 we conclude that:

- For an  $M = 10M_\odot$  binary, the last 25 inspiral cycles, plus the merger and ring-down stages of the waveform contribute only 50% of the signal power, and we need 80 cycles (not shown in the figure) of accurate inspiral waveforms to recover 90% of the signal power. For an  $M = 20M_\odot$  binary, the last 23 cycles, plus the merger and ring-down stages of the waveform contribute  $> 90\%$  of the signal power, and current NR simulations can produce waveforms of such length;
- For an  $M = 30M_\odot$  binary, the last 11 inspiral cycles, plus the merger and ring-down stages of the waveform contribute  $> 90\%$  of the signal power, which means that, for binary systems with total masses higher than  $30M_\odot$ , current NR simulations, e.g., the sixteen cycles obtained in Ref. [38], can provide long enough waveforms for a matched-filter search of binary coalescence, as also found in Ref. [21];
- For an  $M = 100M_\odot$  binary,  $> 90\%$  of the signal power comes from the last inspiral cycle, merger and ring-down stages of the waveform, with two cycles dominating the signal power. It is thus possible to identify this waveform as a “burst” signal.

Similar analyses can be also done for advanced LIGO and VIRGO.

### C. Comparing hybrid waveforms

We shall now compute  $\text{FF}_0$ s between hybrid waveforms. We fix the total mass of the equal-mass binary in each comparison, i.e., we *do not* optimize over mass parameters, but only on phase and time. We use the mismatch, defined as  $1 - \text{FF}_0$ , to measure the difference between waveforms and we compute them for LIGO, advanced LIGO, and VIRGO. Note that by using  $\text{FF}_0$ , we test the closeness among hybrid waveforms that are generated from binary systems with the same physical parameters; in other words, we test whether the waveforms are accurate enough for the purpose of parameter estimation, rather than for the sole purpose of detecting GWs. In the language of Ref. [19] we are studying the *faithfulness* of the PN templates<sup>2</sup>.

Since at late inspiral stages PN waveforms are partly replaced by NR waveforms, differences between hybrid waveforms from two PN models are smaller than those between pure PN waveforms. In general, the more NR cycles we use to generate hybrid waveforms, the less the

difference is expected to be between these hybrid waveforms. This is evident in Figs. 5, 6 where we show mismatches between hybrid waveforms for binary systems with different total masses as a function of the number of NR cycles  $n$ . Specifically, the mismatches are taken between two hybrid waveforms generated from the same NR waveform (from the Goddard group, taking the last  $n$  cycles, plus merger and ring-down) and two different PN waveforms generated with the same masses.

The mismatches are lower for binary systems with higher total masses, since most of their signal power is concentrated in the late cycles close to merger (see Fig. 4). Comparing results between LIGO, advanced LIGO and VIRGO, we see that for the same waveforms the mismatches are lowest when evaluated with the LIGO PSD, and highest when evaluated with the VIRGO PSD. This is due to the much broader bandwidth of VIRGO, especially at low frequency: the absolute sensitivity is not relevant; only the shape of the PSD matters. In VIRGO, the inspiral part of a hybrid waveform has higher weighting in its contribution to the signal power. As already observed at the end of Sec. II, we can see also that the difference between the Epn(3.5) and Tpn(3.5) models is smaller than that between the Tpn(3) and Tpn(3.5) models.

Figures 5, 6 show good agreement among hybrid waveforms. In Sec. IV, as a further confirmation of what was found in Refs. [10, 11], we shall see that PN waveforms from Tpn and Epn models have good agreement with the inspiral phase of the NR waveforms. Therefore, we argue that hybrid waveforms are likely to have high accuracy. In fact, for the late evolution of a compact binary, where NR waveforms are available, the PN waveforms are close to the NR waveforms, while for the early evolution of the binary, where we expect the PN approximations to work better, the PN waveforms (from Tpn and Epn models) are close to each other. Based on these observations, we draw the following conclusions for LIGO, advanced LIGO, and VIRGO data-analysis:

- For binary systems with total mass higher than  $30M_\odot$ , the current NR simulations of equal-mass binary systems (16 cycles) are long enough to reduce mismatches between hybrid waveforms generated from the three PN models to below 0.5%. Since these FFs are achieved without optimizing the binary parameters, we conclude that for these high-mass binary systems, the small difference between hybrid waveforms indicates low systematic error in parameter estimation, i.e., hybrid waveforms are faithful [19].
- For binary systems with total mass around  $10\text{--}20M_\odot$ , 16 cycles of NR waveforms can reduce the mismatch to below 3%, which is usually set as the maximum tolerance for data-analysis purpose (corresponding to  $\sim 10\%$  loss in event rate). By a crude extrapolation of our results, we estimate that with 30 NR waveform cycles, the mismatch might

<sup>2</sup> Following Ref. [19], *faithful* templates are templates that have large overlaps, say  $\gtrsim 96.5\%$ , with the expected signal maximizing *only* over the initial phase and time of arrival. By contrast when the maximization is done *also* on the binary masses, the templates are called *effectual*.

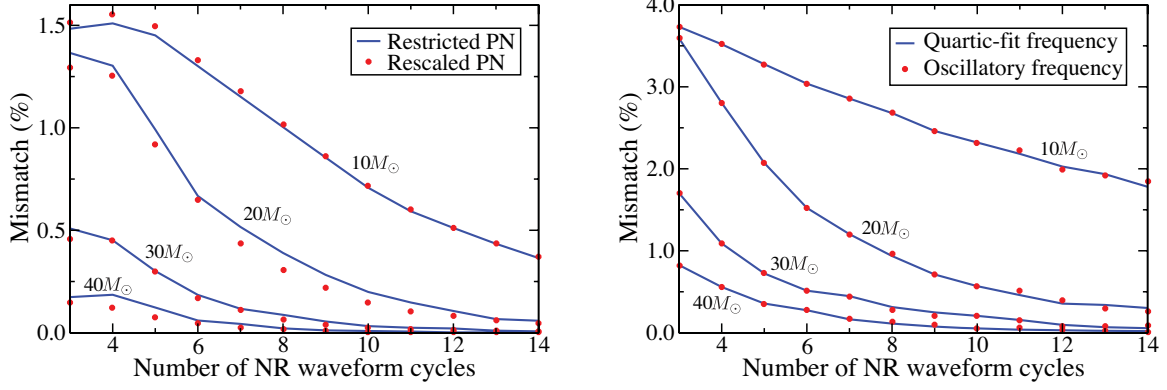


FIG. 5: We show the mismatch between hybrid waveforms as a function of the number of NR waveform cycles used to generate the hybrid waveforms. The LIGO PSD is used to evaluate the mismatches. In the left panel, we compare the Epn(3.5) and Tpn(3.5) models. In the right panel, we compare the Tpn(3) and Tpn(3.5) models. From top to bottom, the four curves correspond to four equal-mass binary systems, with total masses  $10M_\odot$ ,  $20M_\odot$ ,  $30M_\odot$ , and  $40M_\odot$ . The dots show mismatches taken between hybrid waveforms that are generated with different methods. In the left panel, we adjust the amplitude of restricted PN waveforms, such that they connect smoothly in amplitude to NR waveforms. In the right panel, to set the frequency of PN waveforms at the joining point, we use the original orbital frequency, instead of the quartic fitted one. (See Sec. III A for the discussion on amplitude scaling and frequency fitting).

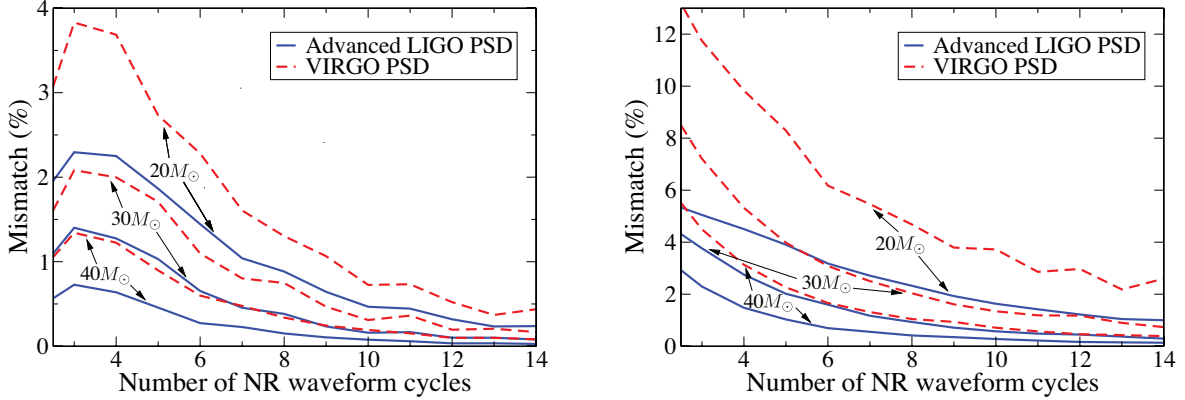


FIG. 6: Mismatch between hybrid waveforms as a function of the number of NR waveform cycles used to generate the hybrid waveforms. Following the settings of Fig. 5, we show comparisons between Epn(3.5) and Tpn(3.5), and Tpn(3) and Tpn(3.5) models in the left and the right panels, respectively. The solid and dashed sets of curves are generated using the PSDs of advanced LIGO and VIRGO. In each set, from top to bottom, the three curves correspond to three equal-mass binary systems, with total masses  $20M_\odot$ ,  $30M_\odot$ , and  $40M_\odot$ .

be reduced to below 1%.

- For binary systems with total mass lower than  $10M_\odot$ , the difference between the Tpn(3) and Tpn(3.5) models is substantial for Advanced LIGO and VIRGO. Their mismatch can be  $> 4\%$  and  $> 6\%$  respectively (not shown in the figure). In this mass range, pursuing more NR waveform cycles in late inspiral phase does not help much, since the

signal power is accumulated slowly over hundreds of GW cycles across the detector band. Nevertheless, here we give mismatches for FF<sub>0</sub>s which are not optimized over binary masses. For the purpose of detection only, optimization over binary parameters leads to low enough mismatches (see also the end of Sec. II). In the language of Ref. [19] hybrid waveforms for total mass lower than  $10M_\odot$  are *ef*-



*fectual* but not faithful.

#### IV. MATCHING NUMERICAL WAVEFORMS WITH POST-NEWTONIAN TEMPLATES

In this section, we compare the complete inspiral, merger and ring-down waveforms of coalescing compact binary systems generated from NR simulations with their best-match PN template waveforms. We also compare hybrid waveforms with PN template waveforms for lower total masses, focusing on the late inspiral phase provided by the NR waveforms. We test seven families of PN templates that either have been used in searches for GWs in LIGO (see e.g., Refs. [40, 41]), or are promising candidates for ongoing and future searches with ground-based detectors. We evaluate the performance of PN templates by computing the FFs maximized on phase, time and binary parameters. As we shall see, for the hybrid waveforms of binary systems with total mass  $M \leq 30M_\odot$ , both the time-domain families Tpn(3.5) and Epn(3.5), which includes a superposition of three ring-down modes, perform well, confirming what found in Refs. [10, 11]. The standard stationary-phase-approximated (SPA) template family in the frequency domain has high FFs only for binary systems with  $M < 20M_\odot$ . After investigating in detail the GW phase in frequency domain, and having understood why it happens (see Sec. IV B 2), we introduce two modified SPA template families (defined in Sec. IV B 2) for binary systems with total mass  $M \geq 30M_\odot$ . Overall, for masses  $M \geq 30M_\odot$ , the Epn(3.5) template family in the time domain and the two modified SPA template families in the frequency domain exhibit the best-match performances.

##### A. Numerical waveforms and post-Newtonian templates

For binary systems with total mass  $M \geq 30M_\odot$ , the last 8–16 cycles contribute more than 80–90% of the signal power, thus in this case we use only the NR waveforms. By contrast, for binary systems with total mass  $10 \leq M \leq 30M_\odot$ , for which the merger and ring-down phases of the waveforms contribute *only*  $\sim 1$ –10%, we use the hybrid waveforms, generated by stitching Tpn waveforms to the Goddard NR waveforms.

We want to emphasize that FFs computed for different target numerical waveforms can not directly be compared with each other. For instance, the Goddard waveform is longer than the Pretorius waveform, and the FFs are sometime slightly lower using the Goddard waveform. This is a completely artificial effect, due to the fact that it is much easier to tune the template parameters and obtain a large FF with a shorter target waveform than a longer one.

We consider seven PN template families. The two time-domain families introduced in Sec. II are:

- Tpn(3.5) [30, 31]: The inspiral Taylor model.

- Epn(3.5) [10, 13, 14, 16, 19]: The EOB model which includes a superposition of three quasi-normal modes (QNMs) of the final BH. These are labeled by three integers  $(l, m, n)$  [42]: the least damped QNM  $(2, 2, 0)$  and two overtones  $(2, 2, 1)$  and  $(2, 2, 2)$ . The ring-down waveform is given as:

$$h_{\text{QNM}}(t) = \sum_{n=0}^2 A_n e^{-(t-t_{\text{end}})/\tau_{22n}} \cos[\omega_{22n}(t-t_{\text{end}}) + \phi_n], \quad (7)$$

where  $\omega_{lmn}$  and  $\tau_{lmn}$  are the frequency and decay time of the QNM  $(l, m, n)$ , determined by the mass  $M_f$  and spin  $a_f$  of the final BH. The quantities  $A_n$  and  $\phi_n$  in Eq. (7) are the amplitude and phase of the QNM  $(2, 2, n)$ . They are obtained by imposing the continuity of  $h_+$  and  $h_\times$ , and their first and second time derivatives, at the time of matching  $t_{\text{match}}$ . Besides the mass parameters, our Epn model contains three other *physical* parameters:  $\epsilon_t$ ,  $\epsilon_M$  and  $\epsilon_J$ . The parameter  $\epsilon_t$  takes into account possible differences between the time  $t_{\text{end}}$  at which the EOB models end and the time  $t_{\text{match}}$  at which the matching to ring-down is done. More explicitly, we set  $t_{\text{match}} = (1+\epsilon_t)t_{\text{end}}$ , and if  $\epsilon_t > 0$ , we extrapolate the EOB evolution, and set an upper limit for the  $\epsilon_t$  search where the extrapolation fails. The parameters  $\epsilon_M$  and  $\epsilon_J$  describe possible differences between the values of the mass  $M_{\text{end}} \equiv E_{\text{end}}$  and angular momentum  $\hat{a}_{\text{end}} \equiv J_{\text{end}}/M_{\text{end}}^2$  at the end of the EOB inspiral and the final BH mass and angular momentum. (The end of the EOB inspiral occurs around the EOB light-ring.) The differences are due to the fact that the system has yet to release energy and angular momentum during the merger and ring-down phase before settling down to the stationary BH solution. If the total binary mass and angular momentum at the end of the EOB inspiral are  $M_{\text{end}}$  and  $J_{\text{end}}$ , we set the total mass and angular momentum of the final stationary BH to be  $M_f = (1 - \epsilon_M)M_{\text{end}}$  and  $J_f = (1 - \epsilon_J)J_{\text{end}}$ , and use  $a_f \equiv J_f/M_f$  to compute  $\omega_{lmn}$  and  $\tau_{lmn}$ . We consider the current Epn model with three parameters  $\epsilon_t$ ,  $\epsilon_M$  and  $\epsilon_J$ , as a first attempt to build a physical EOB model for matching *coherently* the inspiral, merger and ring-down phases. Since the  $\epsilon$ -parameters are related to physical quantities, e.g., the loss of energy during ring-down, they are functions of the initial physical parameters of the binary, such as masses, spins, etc. In the near future we expect to be able to fix the  $\epsilon$ -values by comparing NR and (improved) EOB waveforms for a large range of binary parameters.

We also consider five frequency-domain models, in which two (modified SPA models) are introduced later in Sec. IV B 2, and three are introduced here:

- SPA<sub>c</sub>(3.5) [33]: SPA<sub>c</sub> PN model with an appropriate cutoff frequency  $f_{\text{cut}}$  [30, 31];

	$(5+5)M_\odot$	$(10+10)M_\odot$	$(15+15)M_\odot$
Signal Power (%)	(30, 0.2)	(80, 2)	(85, 10)
$\langle h^{\text{NR-hybr}}, h^{\text{Tpn}(3.5)} \rangle$	0.9875	0.9527	0.8975
$(M/M_\odot, \eta)$	(10.18, 0.2422)	(19.97, 0.2500)	(29.60, 0.2499)
$M\omega_{\text{orb}}$	0.1262	0.1287	0.1287
$\langle h^{\text{NR-hybr}}, h^{\text{Epn}(3.5)} \rangle$	0.9836	0.9522	0.9618
$(M/M_\odot, \eta)$	(10.15, 0.2435)	(19.90, 0.2500)	(29.49, 0.2488)
$(\epsilon_t, \epsilon_M, \epsilon_J)(\%)$	(-0.02, 12.19, 30.87)	(-0.02, 75.03, 95.00)	(0.05, 2.38, 92.06)
$M\omega_{\text{orb}}$	0.1346	0.1345	0.1345
$\langle h^{\text{NR-hybr}}, h^{\text{SPA}_c(3.5)} \rangle$	0.9690	0.9290	0.8355
$(M/M_\odot, \eta)$	(10.16, 0.2432)	(19.93, 0.2498)	(29.08, 0.2500)
$(f_{\text{cut}}/\text{Hz})$	1566.8	263.9	529.6

TABLE I: FFs between hybrid waveforms [Tpn(3.5) waveform stitched to the Goddard waveform] and PN templates. In the first row, the two numbers in parentheses are the percentages of the signal-power contribution from the 16 inspiraling NR cycles and the NR merger/ring-down cycles. (The separation between inspiral and merger/ring-down is obtained using the EOB approach as a guide, i.e., we match the Epn(3.5) model and use the EOB light-ring position as the beginning of the merger phase.) In the PN-template rows, the first number in each block is the FF, and the numbers in parentheses are template parameters that achieve this FF. The last number in each block of the Tpn(3.5) and Epn(3.5) models is the ending orbital frequency of the best-match template. For the Epn model, the ending frequency is computed at the point of matching with the ring-down phase, around the EOB light ring.

- BCV [31]: BCV model with an amplitude correction term  $(1 - \alpha f^{2/3})$  and an appropriate cutoff frequency  $f_{\text{cut}}$ .

- BCV<sub>impr</sub> [31]: Improved BCV model with an amplitude correction term  $(1 - \alpha f^{1/2})$  and an appropriate cutoff frequency  $f_{\text{cut}}$ . We include this improved BCV model because Ref. [10] found a deviation of the Fourier-transform amplitude from the Newtonian prediction  $f^{-7/6}$  during the merger and ring-down phases (see Fig. 22 of Ref. [10]). Here we shall assume  $n = -2/3$  in the  $f^n$  power law to get the  $(1 - \alpha f^{1/2})$  form of the amplitude correction. While it was found [10] that the value of  $n$  is close to  $-2/3$  for the  $l = 2, m = 2$  waveform, this value varies slightly if other multiple moments are included and if binary systems with different mass ratios are considered. Finally, the  $\alpha$  parameter is expected to be negative, but in our actual search it can take both positive and negative values.

## B. Discussion of fitting-factor results

In Table I, we list the FFs for hybrid target waveforms and three PN template families: Tpn(3.5), Epn(3.5), and SPA<sub>c</sub>(3.5), together with the template parameters at which the best match is obtained. As shown in the first row, in this relatively low-mass range, i.e.  $10M_\odot < M < 30M_\odot$ , the merger/ring-down phases of the waveforms contribute only a small fraction of the total signal power, while the last 16 inspiraling cycles of the NR waveform contribute a significant fraction. Therefore, confirming recent claims by Refs. [10, 11], we can conclude that the PN template families Tpn(3.5) and Epn(3.5) have good agreement with the inspiraling NR waveforms. The Tpn(3.5) model gives a low FF for  $M = 30M_\odot$  because

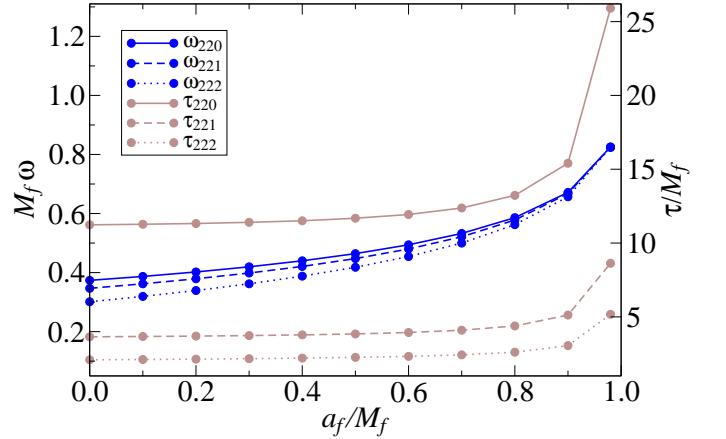


FIG. 7: Frequencies and decay times of the least damped QNM 220, and two overtones 221 and 222. The scales of the frequency and the decay time are listed on the left and right sides of the plot, respectively.

for these higher masses the merger/ring-down phases, which the Tpn model does not include, start contributing to the signal power. Note that both time-domain templates give fairly good estimates of the mass parameters. The SPA<sub>c</sub>(3.5) template family gives FFs that drop substantially when the total binary mass increases from  $10M_\odot$  to  $30M_\odot$ , indicating that this template family can only match the early, less relativistic inspiral phase of the hybrid waveforms. Nevertheless, it turns out that by slightly modifying the SPA waveform we can match the NR waveforms with high FFs (see Sec. IV B 2).

In Table II, we list the FFs for full NR waveforms and five PN template families: Epn(3.5), SPA<sub>c</sub><sup>ext</sup>(3.5), SPA<sub>c</sub><sup>y</sup>(4), BCV, and BCV<sub>impr</sub>, together with the tem-

	$(15 + 15)M_\odot$	$(20 + 20)M_\odot$	$(30 + 30)M_\odot$	$(50 + 50)M_\odot$
$\langle h^{\text{NR-Pretorius}}, h^{\text{Epn}(3.5)} \rangle$	0.9616	0.9599	0.9602	0.9787
$(M/M_\odot, \eta)$	(27.93, 0.2384)	(35.77, 0.2426)	(52.27, 0.2370)	(96.60, 0.2386)
$(\epsilon_t, \epsilon_M, \epsilon_J)(\%)$	(-0.08, 0.63, 99.70)	(-0.03, 0.48, 94.38)	(-0.12, 0.00, 64.14)	(0.04, 0.01, 73.01)
$\langle h^{\text{NR-Pretorius}}, h^{\text{SPA}^{\text{ext}}(3.5)} \rangle$	0.9712	0.9802	0.9821	0.9722
$(M/M_\odot, \eta)$	(19.14, 0.8037)	(24.92, 0.9097)	(36.75, 0.9933)	(58.06, 0.9986)
$(f_{\text{cut}}/\text{Hz})$	(589.6)	(476.9)	(318.9)	(195.9)
$\langle h^{\text{NR-Pretorius}}, h^{\text{SPA}^{\text{Y}}(4)} \rangle$	0.9736	0.9824	0.9874	0.9851
$(M/M_\odot, \eta)$	(29.08, 0.2460)	(38.63, 0.2461)	(57.58, 0.2441)	(96.55, 0.2457)
$(f_{\text{cut}}/\text{Hz})$	(666.5)	(501.2)	(332.5)	(199.4)
$\langle h^{\text{NR-Pretorius}}, h^{\text{BCV}} \rangle$	0.9726	0.9807	0.9788	0.9662
$(\psi_0/10^4, \psi_1/10^2)$	(2.101, 1.655)	(1.178, 1.744)	(0.342, 2.385)	(-0.092, 3.129)
$(10^2\alpha, f_{\text{cut}}/\text{Hz})$	(-1.081, 605.5)	(-0.834, 461.7)	(0.162, 320.4)	(1.438, 204.3)
$\langle h^{\text{NR-Pretorius}}, h^{\text{BCV}_{\text{impr}}} \rangle$	0.9727	0.9807	0.9820	0.9803
$(\psi_0/10^4, \psi_1/10^2)$	(2.377, 0.930)	(1.167, 1.762)	(0.431, 2.077)	(-0.109, 3.158)
$(10^2\alpha, f_{\text{cut}}/\text{Hz})$	(-3.398, 571.9)	(-2.648, 458.3)	(-1.196, 319.1)	(-3.233, 196.0)

	$(15 + 15)M_\odot$	$(20 + 20)M_\odot$	$(30 + 30)M_\odot$	$(50 + 50)M_\odot$
$\langle h^{\text{NR-Goddard}}, h^{\text{Epn}(3.5)} \rangle$	0.9805	0.9720	0.9692	0.9671
$(M/M_\odot, \eta)$	(29.25, 0.2435)	(38.27, 0.2422)	(56.66, 0.2381)	(83.52, 0.2233)
$(\epsilon_t, \epsilon_M, \epsilon_J)(\%)$	(0.05, 0.03, 99.90)	(0.05, 0.27, 99.17)	(0.09, 0.01, 54.56)	(0.10, 1.71, 79.75)
$\langle h^{\text{NR-Goddard}}, h^{\text{SPA}^{\text{ext}}(3.5)} \rangle$	0.9794	0.9785	0.9778	0.9693
$(M/M_\odot, \eta)$	(21.41, 0.5708)	(27.27, 0.6695)	(37.67, 0.9911)	(60.90, 0.9947)
$(f_{\text{cut}}/\text{Hz})$	(552.7)	(444.4)	(318.5)	(191.7)
$\langle h^{\text{NR-Goddard}}, h^{\text{SPA}^{\text{Y}}(4)} \rangle$	0.9898	0.9905	0.9885	0.9835
$(M/M_\odot, \eta)$	(30.28, 0.2456)	(40.23, 0.2477)	(60.54, 0.2455)	(100.00, 0.2462)
$(f_{\text{cut}}/\text{Hz})$	(674.6)	(506.6)	(330.5)	(195.0)
$\langle h^{\text{NR-Goddard}}, h^{\text{BCV}} \rangle$	0.9707	0.9710	0.9722	0.9692
$(\psi_0/10^4, \psi_1/10^2)$	(3.056, -1.385)	(1.650, -0.091)	(0.561, 1.404)	(-0.113, 3.113)
$(10^2\alpha, f_{\text{cut}}/\text{Hz})$	(0.805, 458.3)	(0.559, 412.6)	(0.218, 309.2)	(1.063, 198.7)
$\langle h^{\text{NR-Goddard}}, h^{\text{BCV}_{\text{impr}}} \rangle$	0.9763	0.9768	0.9782	0.9803
$(\psi_0/10^4, \psi_1/10^2)$	(2.867, -0.600)	(1.514, 0.448)	(0.555, 1.425)	(-0.165, 3.373)
$(10^2\alpha, f_{\text{cut}}/\text{Hz})$	(0.193, 578.0)	(-1.797, 441.1)	(-4.472, 308.1)	(-4.467, 193.4)

TABLE II: FFs between NR waveforms and PN templates which include merger and ring-down phases. The upper table uses Pretorius' waveform, and the lower table uses Goddard's high-resolution long waveform. The first number in each block is the FF, and numbers in parentheses are template parameters that achieve this FF.

plate parameters at which the best match is obtained. The  $\text{SPA}_c^{\text{ext}}(3.5)$  and  $\text{SPA}_c^{\text{Y}}(4)$  families are modified versions of the SPA family, defined in Sec. IV B 2.

We shall investigate these results in more detail in the following sections.

### 1. Effective-one-body template performances

The Epn model is the only available time-domain model that explicitly includes ring-down waveforms. It achieves high FFs  $\geq 0.96$  for all target waveforms, confirming the necessity of including ring-down modes and proving that the inclusion of three QNMs with three tuning parameters  $\epsilon_t$ ,  $\epsilon_M$  and  $\epsilon_J$  is sufficient for detection. As we see in Table II, the values of the tuning parameters  $\epsilon_M$  and  $\epsilon_J$ , where the FFs are achieved, are different from their physical values. For reference, the Goddard numerical simulation predicts  $M_f \simeq 0.95M$

and  $\hat{a}_f \equiv J_f/M_f^2 \simeq 0.7$  [38], and Epn(3.5) predicts  $M_{\text{end}} = 0.967$  and  $\hat{a}_{\text{end}} \equiv J_{\text{end}}/M_{\text{end}}^2 = 0.796$ , so the two tuning parameters should be  $\epsilon_M \simeq 1.75\%$  and  $\epsilon_J \simeq 11\%$ . In our search, e.g., for  $M = 30M_\odot$ ,  $\epsilon_J$  tends to be tuned to its lowest possible value and  $\epsilon_t$  tends to take its highest possible value, indicating that pushing the end of the Epn(3.5) inspiral to a later time gives higher FFs.

Since the parameters  $\epsilon_M$  and  $\epsilon_J$  depend on the QNM frequency and decay time, we show in Fig. 7 how  $\omega_{lmn}$  and  $\tau_{lmn}$  vary as functions of  $a_f$  [42] for the three modes used in the Epn(3.5) model. The frequencies  $\omega_{lmn}$  of the three modes are not really different, and grow monotonically with increasing  $a_f$ . The decay times  $\tau_{lmn}$ , although different for the three modes, also grow monotonically with increasing  $a_f$ . Thus, the huge loss of angular momentum  $\epsilon_J$ , or equivalently the small final BH spin required in the Epn(3.5) model to achieve high FFs, indicates that *low* ring-down frequencies and/or *short* decay times are needed for this model to match the numerical

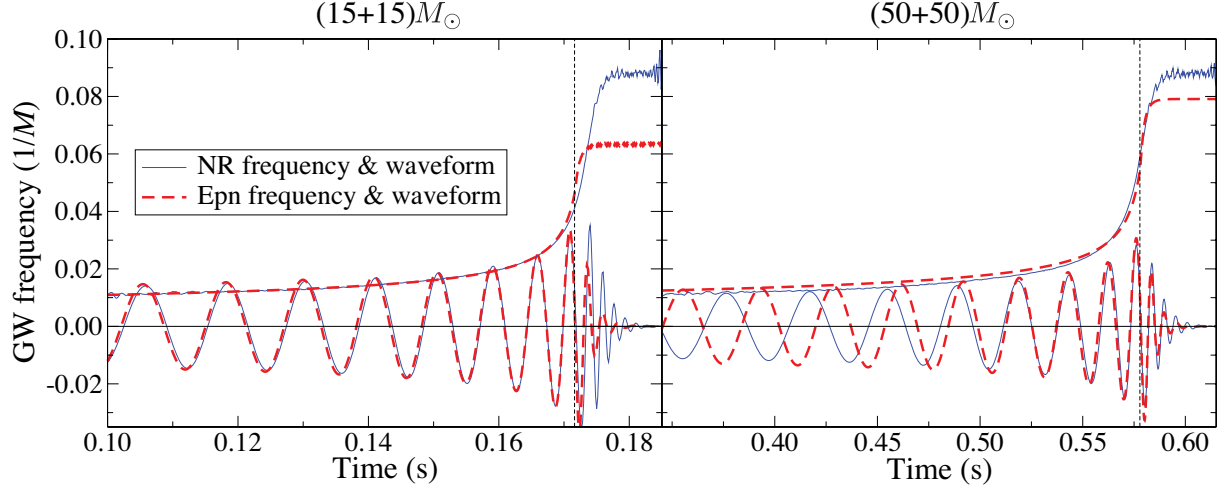


FIG. 8: Frequency evolution of waveforms from the Epn(3.5) model, and the NR simulations of the Goddard group. In the left and right panels, we show frequency evolutions for two equal-mass binary systems with total mass  $30M_\odot$  and  $100M_\odot$ . In each panel, there are two nearly monotonic curves and two oscillatory curves, where the former are frequency evolutions and the latter are binary coalescence waveforms. The solid curves (blue) are from the NR simulations, while the dashed curves (red) are from the Epn(3.5) model. The vertical line in each plot shows the position where the three-QNM ring-down waveform is attached to the EOB waveform.

merger and ring-down waveforms.

In Fig. 8, we show Goddard NR and Epn(3.5) waveforms, as well as their frequency evolutions, for two equal-mass binary systems with total masses  $30M_\odot$  and  $100M_\odot$ . In the low-mass case, i.e.,  $M = 30M_\odot$ , since the inspiral part contributes most of the SNR, the Epn(3.5) model fits the frequency and phase evolution of the NR inspiral well, with the drawback that at the joining point the EOB frequency is substantially higher than that of the NR waveform. Then, in order to fit the early ring-down waveform which has higher amplitude, the tuning parameters have to take values in Table II such that the ring-down frequency is small enough to get close to the NR frequency during *early* ring-down stage, as indicated in Fig. 8. The late ring-down waveform does not contribute much to the SNR, and thus it is not too surprising that waveform optimizing the FF does not adequately represent this part of the NR waveform. In the higher mass case,  $M = 100M_\odot$ , the Epn(3.5) model gives a much better, though not perfect, match to the merger and ring-down phases of the NR waveform, at the expense of misrepresenting the early inspiral part. Again, this is not unexpected considering that in this mass range the merger and ring-down waveforms dominate the contribution to the SNR.

Comparing the two cases discussed above, we can see that with the current procedure of matching the inspiral and ring-down waveforms in the EOB approach it is not possible to obtain a perfect match with the entire NR waveform. However, due to the limited detector sensitivity bandwidth, the FFs are high enough for detection.

The large systematic error in estimating the physical parameters will be overcome by improving the EOB matching procedure during the inspiral part, and also by fixing the  $\epsilon$ -parameters to physical values obtained by comparison with numerical simulations.

Finally, in Figs. 9, 10 we show the frequency-domain amplitude and phase of the NR and EOB waveforms. Quite interestingly, we notice that the inclusion of three ring-down modes reproduce rather well the *bump* in the NR frequency-domain amplitude. The EOB frequency-domain phase also matches the NR one very well.

## 2. Stationary-phase-approximated template performances

Figures 9, 10 also show the frequency-domain phases and amplitudes for the best-match  $\text{SPA}_c(3.5)$  waveforms. We see that at high frequency the NR and  $\text{SPA}_c(3.5)$  phases rise with different slopes<sup>3</sup>. Based on this observation we introduce two modified SPA models:

- $\text{SPA}_c^{\text{ext}}(3.5)$ :  $\text{SPA}_c$  PN model with unphysical values of  $\eta$  and an appropriate cutoff frequency  $f_{\text{cut}}$ . The range of the symmetric mass-ratio  $\eta = m_1 m_2 / (m_1 + m_2)^2$  is extended from its physical range  $0 \sim 0.25$  to the unphysical

<sup>3</sup> By looking in detail at the PN terms in the  $\text{SPA}_c(3.5)$  phase, we find that the difference in slope is largely due to the logarithmic term at 2.5PN order.



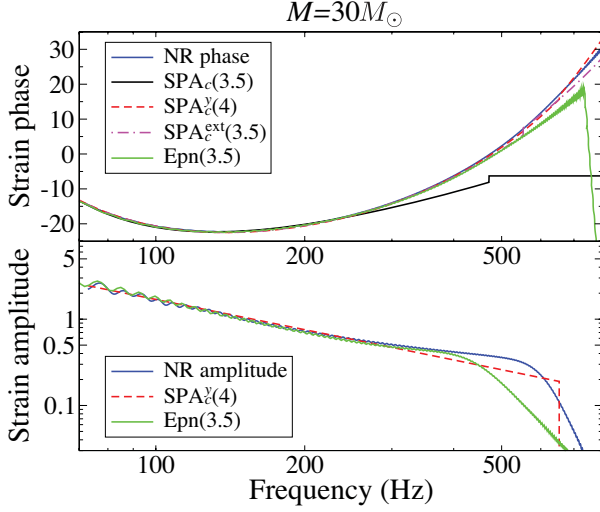


FIG. 9: For  $M = 30M_\odot$  equal-mass binary systems, we compare the phase and amplitude of the frequency-domain waveforms from the  $\text{SPA}_c$  models and NR simulation (Goddard group). We also show the amplitude of the waveform from the  $\text{Epn}(3.5)$  model.

range  $0 \sim 1$ .

- $\text{SPA}_c^Y(4)$ :  $\text{SPA}_c$  PN model with an *ad hoc* 4PN order term in the phase, and an appropriate cutoff frequency  $f_{\text{cut}}$ . The phase of the SPA model is known up to the 3.5PN order (see, e.g., Eq. (3.3) of Ref. [33]):

$$\psi(f) = 2\pi f t_0 - \phi_0 - \frac{\pi}{4} + \frac{3}{128\eta v^5} \sum_{k=0}^N \alpha_k v^k, \quad (8)$$

where  $v = (\pi M f)^{1/3}$ . The PN coefficients  $\alpha_k$ s,  $k = 0, \dots, N$ , (with  $N = 7$  at 3.5PN order) are given by Eqs. (3.4a), (3.4h) of Ref. [33]. We add the following term at 4PN order:

$$\alpha_8 = \mathcal{Y} \log v, \quad (9)$$

where  $\mathcal{Y}$  is a parameter which we fix by imposing high matching performances with NR waveforms. Note that a constant term in  $\alpha_8$  only adds a 4PN order term that is linear in  $f$ , which can be absorbed into the  $2\pi f t_0$  term. Thus, to obtain a nontrivial effect, we need to introduce a logarithmic term. The coefficient  $\mathcal{Y}$  could in principle depend on  $\eta$ . We determine  $\mathcal{Y}$  by optimizing the FFs of equal and unequal masses. We find that in the equal-mass case  $\mathcal{Y}$  does not depend significantly on the binary total mass and is given by  $\mathcal{Y} = 3923$ . The latter is also close to the best match value obtained for unequal masses. More specifically, it is within 4.5% for binary systems of mass ratio  $m_2/m_1 = 2$ . To further explore the dependence of  $\mathcal{Y}$  on  $\eta$ , we need a larger sample of waveforms

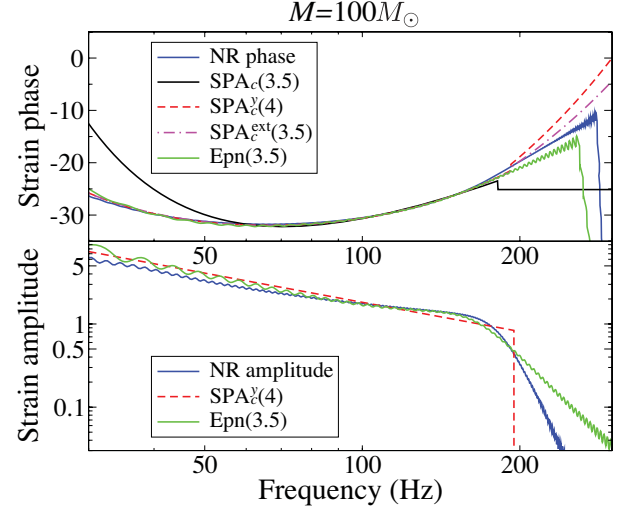


FIG. 10: For  $M = 100M_\odot$  equal-mass binary systems, we compare the phase and amplitude of the frequency-domain waveforms from the  $\text{SPA}_c$  models and NR simulation (Goddard group). We also show the amplitude of the waveform from the  $\text{Epn}(3.5)$  model.

for unequal-mass binary systems<sup>4</sup>. As seen in Table II, the two modified  $\text{SPA}_c$  template families have  $\text{FF} > 0.97$  (except for one 0.9693) for all target waveforms, even though no explicit merger or ring-down phases are included in the waveform. The  $\text{SPA}_c^Y(4)$  model provides also a really good estimation of parameters.

In Fig. 11 we plot Goddard NR and  $\text{SPA}_c^Y(4)$  waveforms for two equal-mass binary systems with total masses  $M = 30M_\odot$  and  $M = 100M_\odot$ . We can clearly see tail-like ring-down waveforms at the end of the  $\text{SPA}_c^Y(4)$  waveforms, which result from the inverse Fourier transform of frequency domain waveforms that have been cut at  $f = f_{\text{cut}}$ . This well-known feature is called the Gibbs phenomenon. At first glance, it may appear surprising that the often inconvenient Gibbs phenomenon [44] can provide reasonable ring-down waveforms in the time domain. However, by looking at the spectra of these waveforms in the frequency domain (see the amplitudes in Figs. 9 & 10), we see that the  $\text{SPA}_c^Y(4)$  cuts off at the frequency  $f_{\text{cut}}$  (obtained from the optimized FF) where the NR spectra also start to drop. Thus, even though the frequency-domain  $\text{SPA}_c$  waveforms are discontinuous, while the frequency-domain NR waveforms are continuous (being combinations of Lorentzians), the  $\text{SPA}_c$  time-domain waveforms contain tails with frequencies and decay rates similar to the NR ring-down modes. We expect that the values of the cutoff frequency  $f_{\text{cut}}$  at which the FFs are maximized are well-determined by

<sup>4</sup> Note that the *auxiliary phase* introduced in Eq. (239) of Ref. [43] also gives rise to a term in the SPA phase of the kind  $f \log v$ , except an order of magnitude smaller than  $\mathcal{Y}$ .

the highest frequency of the NR waveforms, i.e. by the frequency of the fundamental QNM. In the next section, we shall show quantitative results to confirm this guess.

### 3. Buonanno-Chen-Vallisneri template performances

In Table II we see that the BCV and  $\text{BCV}_{\text{impr}}$  families give almost the same FFs for relatively low-mass binary systems ( $M = 30, 40M_{\odot}$ ), while the  $\text{BCV}_{\text{impr}}$  family gives slightly better FFs for higher mass binary systems ( $M = 60, 100M_{\odot}$ ). For higher-mass binary systems, we find that the  $\alpha$  parameter takes negative values with reasonable magnitude. This is because the amplitude of the NR waveforms in the frequency domain deviates from the  $f^{-7/6}$  power law only near the merger, which lasts for about *one* GW cycle. This merger cycle is important only when the total mass of the binary is high enough (see Fig. 4). [See also Ref. [46] where similar tests have been done.]

The BCV and  $\text{BCV}_{\text{impr}}$  template families give FFs nearly as high as those given by the  $\text{SPA}_c^{\mathcal{Y}}(4)$  family, but the latter has the advantage of being parametrized directly in terms of the physical binary parameters, and it gives fairly small systematic errors.

### C. Frequency-domain templates for inspiral, merger and ring-down

In this section, we extend our comparisons between the  $\text{SPA}_c$  families and NR waveforms to higher total-mass binary systems ( $40M_{\odot}$  to  $120M_{\odot}$ ) and to unequal-mass binary systems with mass-ratios  $m_2/m_1 = 1.5$  and 2. The numerical simulations for unequal-mass binary systems are from the Goddard group. They last for  $\simeq 373M$  and  $\simeq 430M$ , respectively, and the NR waveforms have  $\simeq 4$  cycles before the merger.

In Figs. 12 and 13 we show the FFs for  $\text{SPA}_c^{\text{ext}}(3.5)$  and  $\text{SPA}_c^{\mathcal{Y}}(4)$  templates, and the values of  $f_{\text{cut}}$  that achieved these FFs<sup>5</sup>. For all mass combinations (except for  $M = 40M_{\odot}$  for artificial reasons) the FFs of  $\text{SPA}_c(3.5)$  templates are higher than 0.96, and the FFs of  $\text{SPA}_c^{\mathcal{Y}}(4)$  templates are higher than 0.97, confirming that both families of templates can be used to search for GWs from coalescing binary systems with equal-masses as large as  $120M_{\odot}$  and mass ratios  $m_2/m_1 = 2$  and 1.5. Figure 13 shows that all the  $f_{\text{cut}}$  values from our searches

are within 10% larger than the frequency of the fundamental QNM  $\omega_{220}$  of an equal-mass binary. We have checked that if we fix  $f_{\text{cut}} = 1.07\omega_{220}/2\pi$ , the FFs drop by less than 1%.

In Fig. 15, we show the same information as in Fig. 7, except that here we draw  $\omega_{l_{nm}}$  and  $\tau_{l_{nm}}$  as functions of the mass-ratio  $\eta$  of a nonspinning binary. We compute the spin of the final BH in units of the mass of the final BH using the quadratic fit given by Eq. (3.17a) of Ref. [47]:

$$\frac{a_f}{M_f} \simeq 3.352\eta - 2.461\eta^2. \quad (10)$$

As Fig. 15 shows,  $\omega_{220}$  does not change much, confirming the insensitivity of the  $f_{\text{cut}}$  on  $\eta$ .

However, in real searches we might request that the template family have some deviations from the waveforms predicted by NR. For example, a conservative template bank might cover a region of  $f_{\text{cut}}$  ranging from the Schwarzschild innermost stable circular orbit (ISCO) frequency, or the innermost circular orbit (ICO) frequency determined by the 3PN conservative dynamics, up to a value slightly higher than the frequency of the fundamental QNM. The number of templates required to cover the  $f_{\text{cut}}$  dimension depends on the binary masses. We find that to cover the  $f_{\text{cut}}$  dimension from the 3PN ICO frequency to the fundamental QNM frequency with an  $\text{SPA}_c^{\text{ext}}(3.5)$  template bank, imposing a mismatch  $< 0.03$  between neighboring templates, we need only two ( $\sim 20$ ) templates if  $M = 30M_{\odot}$  ( $M = 100M_{\odot}$ ) and  $\eta = 0.25$ . In the latter case, the match between templates is more sensitive to  $f_{\text{cut}}$  since most signal power comes from the last two cycles, sweeping through a large frequency range, right in LIGO's most sensitive band. The number of templates directly affects the computational power needed, and the false-alarm rate. Further investigations are needed in order to determine the most efficient way to search over the  $f_{\text{cut}}$  dimension.

For the purpose of parameter estimation, Fig. 14 shows that the  $\text{SPA}_c^{\mathcal{Y}}(4)$  templates are rather faithful, giving reasonable estimates of the chirp mass: systematic errors less than about 8% in absolute value for binary systems with  $M = 40M_{\odot}$  up to  $M = 120M_{\odot}$ . A difference of  $\simeq 8\%$  may seem large, but the  $\text{SPA}_c^{\mathcal{Y}}(4)$  templates are not exactly physical, and more importantly, for large-mass binary systems, most of the information on the chirp mass comes *only* from the last cycle of inspiral. We notice that when the total binary mass is higher than  $120M_{\odot}$ , the FFs are relatively high (from 0.93 to 0.97), and the estimates of the chirp mass are still good (within 10%). However, for binary systems with such high total masses, the ring-down waveform dominates the SNR, and the  $\text{SPA}_c^{\mathcal{Y}}(4)$  template family becomes purely phenomenological. A direct ring-down search might be more efficient.

All results for unequal-mass binary systems are obtained using the  $C_{22}$  component of  $\Psi_4$  [10], which is the leading order quadrupole term contributing to the

<sup>5</sup> Note that because of the short NR waveforms for unequal-mass binary systems, we need to search over the starting frequency of templates with a coarse grid, and this causes some oscillations in our results. The oscillations are artificial and will be smoothed out in real searches. For instance, the drop of FFs at  $40M_{\odot}$  for unequal-mass binary systems happens because the NR waveforms are too short and begin right in the most sensitive band of LIGO.

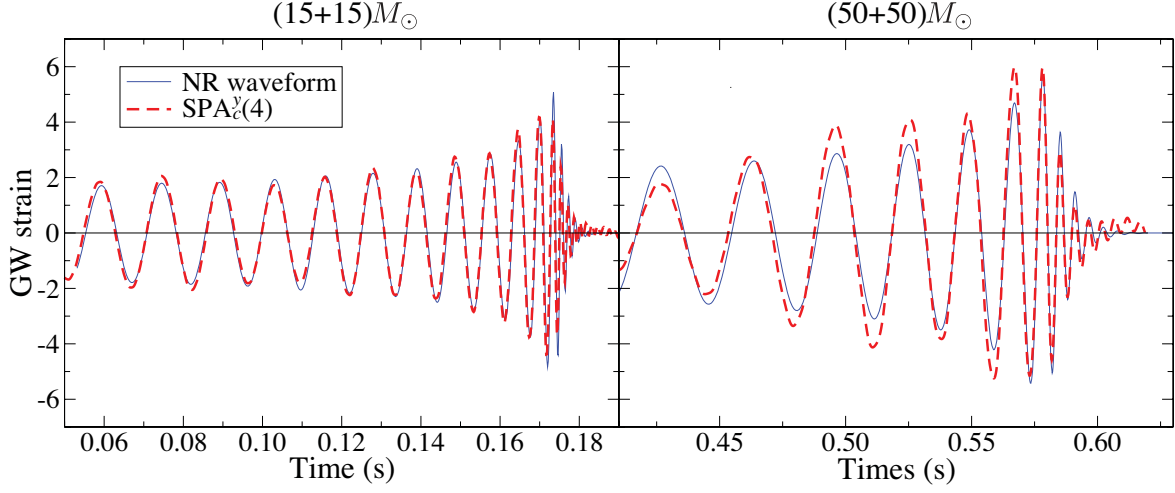


FIG. 11: Binary coalescence waveforms from the  $\text{SPA}_c^\gamma(4)$  model, and the NR simulations of the Goddard group. In the left and right panels we show waveforms for two equal-mass binary systems with total mass  $30M_\odot$  and  $100M_\odot$ . The solid lines show the waveforms from the NR simulation, and the dashed lines give the best-matching waveforms from the  $\text{SPA}_c^\gamma(4)$  model.

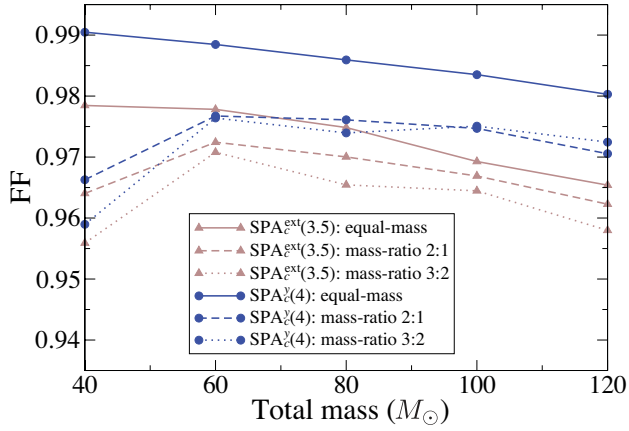


FIG. 12: FFs as functions of the total binary mass. The FFs are computed between either the  $\text{SPA}_c^{\text{ext}}(3.5)$  or the  $\text{SPA}_c^\gamma(4)$  templates and the NR waveforms for equal-mass and unequal-mass binary systems.

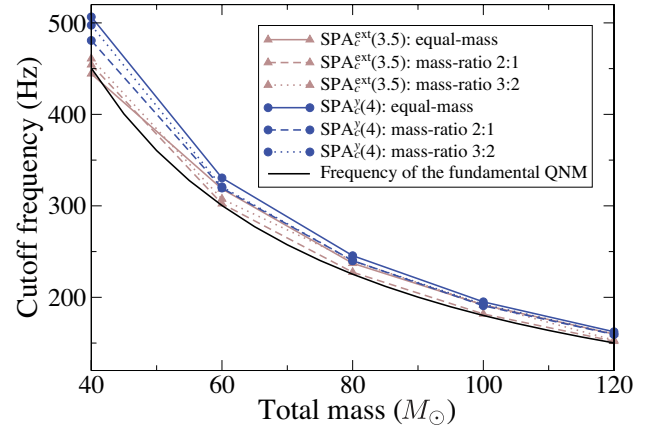


FIG. 13: Cutoff frequencies as functions of the total binary mass. We show the best-match  $f_{\text{cut}}$  for  $\text{SPA}_c^{\text{ext}}(3.5)$  and  $\text{SPA}_c^\gamma(4)$  templates of Fig. 12. The solid black curve is the fundamental QNM frequency  $\omega_{220}/2\pi$ . The frequencies are in units of Hz.

GW radiation. For unequal-mass binary systems, higher-order multipoles can also be important, and we need to test the performance of the template family directly using  $\Psi_4$ . For  $\Psi_4$  extracted in the direction perpendicular to the binary orbit, we verified that higher-order multipoles do not appreciably change the FFs.

A natural way of improving the  $\text{SPA}_c$  models would be to replace the discontinuous frequency cut with a linear combination of Lorentzians. We show here a first attempt

at doing so. The Lorentzian  $\mathcal{L}$  is obtained as a Fourier transform of a damped sinusoid, e.g., for the fundamental QNM we have

$$\int_{-\infty}^{\infty} e^{i2\pi ft} \left( e^{\pm i\omega_{220}t - |t|/\tau_{220}} \right) dt = \frac{2/\tau_{220}}{1/\tau_{220}^2 + (2\pi f \pm \omega_{220})^2} \equiv 2\mathcal{L}_{220}^\pm(f) \quad (11)$$

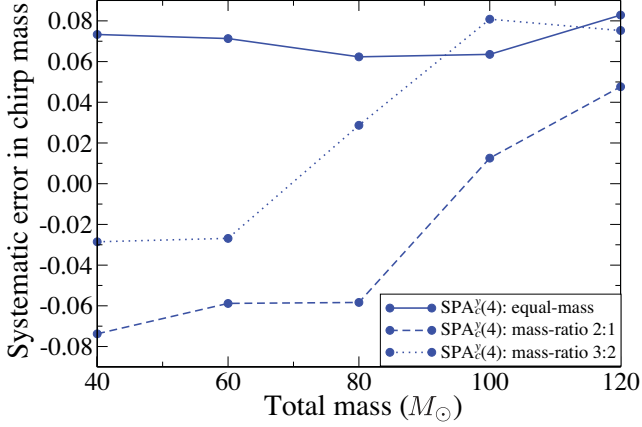


FIG. 14: Systematic errors of the chirp mass as functions of the total binary mass when  $\text{SPA}_c^y(4)$  templates are used. We show errors of the chirp masses that optimize the FFs of Fig. 12.

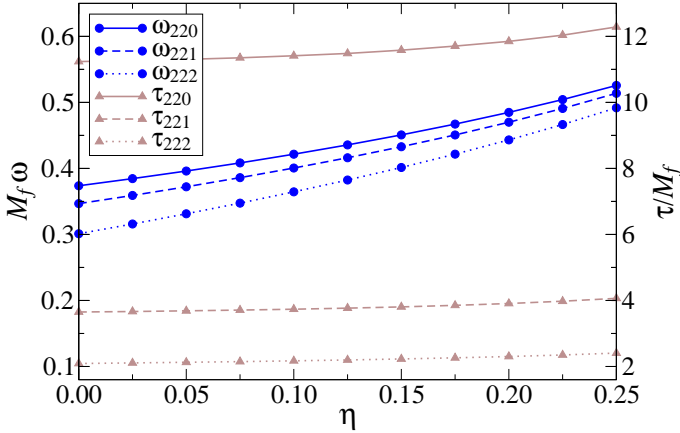


FIG. 15: Frequencies and decay times of the least damped QNM 220, and two overtones 221 and 222. The scales of the frequency and the decay time are listed on the left and right sides of the plot, respectively.

and the (inverse) Fourier transform of Eq. (7) reads

$$\sum_n \tilde{h}_{\text{QNM}}(f) = A_n [\mathcal{L}_{22n}^+(f) e^{i\phi_n} + \mathcal{L}_{22n}^-(f) e^{-i\phi_n}] . \quad (12)$$

Restricting to positive frequencies we only keep the  $\mathcal{L}_{22n}^-(f)$  terms. In the frequency domain we attach the fundamental mode continuously to the  $\text{SPA}_c^y(4)$  waveform at the ring-down frequency  $\omega_{220}$  by tuning the amplitude and phase  $A_0$  and  $\phi_0$ . We denote this model

$\text{SPA}_{\mathcal{L}1}$  (note that we also need to introduce the mass-parameter of the final BH as a scale for  $\omega_{220}$  and  $\tau_{220}$ ). Similarly, we define the  $\text{SPA}_{\mathcal{L}3}$  model where all three QNMs are combined. With the three amplitudes and phases as parameters, this model is similar to the spin-BCV template family [30] and we can optimize automatically over the 6 parameters. As an example, we compute the FFs between the  $\text{SPA}_{\mathcal{L}1}(4)$  or  $\text{SPA}_{\mathcal{L}3}(4)$  and the NR waveform of an equal-mass  $M = 100M_\odot$  binary. Using the LIGO PSD, we obtain 0.9703 and 0.9817, respectively. Those FFs are comparable to the FFs obtained with the simpler  $\text{SPA}_c$  model, shown in Fig. 12. It is known that adding more parameters increases the FFs but also increases the false-alarm probability. By further investigation and comparison with NR waveforms our goal is to express the phase and amplitude parameters of the Lorentzian in terms of the physical binary parameters, relating them to the amplitudes and phases of the QNMs and the physics of the merger. Those parameters are somewhat similar to the  $\epsilon$ -parameters introduced above for the EOB model when modeling the merger and ring-down phases.

We wish to emphasize that the results we presented in this section are preliminary, in the sense that we considered only a few mass combinations and the NR waveforms of unequal-mass binary systems are quite short. Nevertheless, these results are interesting enough to propose a systematic study of the efficiency of these template families through Monte Carlo simulations in real data.

## V. CONCLUSIONS

In this paper we compared NR and analytic waveforms emitted by nonspinning binary systems, trying to understand the performance of PN template families developed during the last ten years and currently used for the search for GWs with ground-based detectors, suggesting possible improvements.

We first computed FF<sub>0</sub>s (maximized only on time and phase) between PN template families which best match NR waveforms [10, 11], i.e., Tpn(3), Tpn(3.5) and Epn(3.5). We showed how the drop in FF<sub>0</sub>s is not simply determined by the accumulated phase difference between waveforms, but also depends on the detector's PSD and the binary mass. Thus, waveforms which differ even by one GW cycle can have  $\text{FF}_0 \sim 0.97$ , depending on the binary masses (see Fig. 1).

We then showed that the NR waveforms from the high-resolution and medium-resolution simulations of the Goddard group are close to each other ( $\text{FF}_0$  around 0.99, see Fig. 2). We also estimated that the  $\text{FF}_0$  between high-resolution and exact NR waveforms is even higher, based on the numerical convergence rates of the Goddard simulations.

Second, by stitching PN waveforms to NR waveforms we built hybrid waveforms, and computed FF<sub>0</sub>s (maximized only on time and phase) between hybrid wave-



forms constructed with different PN models, notably Tpn(3), Tpn(3.5) and Epn(3.5) models. We found that for LIGO's detectors and equal-mass binary systems with total mass  $M > 30M_\odot$ , the last 11 GW cycles plus merger and ring-down phases contribute  $> 90\%$  of the signal power. This information can be used to set the length of NR simulations.

The FF<sub>0</sub>s between hybrid waveforms are summarized in Figs. 5, 6. We found that for LIGO's detectors and binary systems with total mass higher than  $10M_\odot$ , the current NR simulations for equal-mass binary systems are long enough to reduce the differences between hybrid waveforms built with the PN models Tpn(3), Tpn(3.5) and Epn(3.5) to the level of  $< 3\%$  mismatch. For GW detectors with broader bandwidth like advanced LIGO and VIRGO, longer NR simulations will be needed if the total binary masses  $M < 10M_\odot$ . With the current available length of numerical simulations, it is hard to estimate from the FFs between hybrid waveforms how long the simulations should be. Nevertheless, from our study of the distribution of signal power, we estimate that for  $M < 10M_\odot$  binary systems, at least  $\sim 80$  NR inspiraling cycles before merger are needed.

Finally, we evaluated FFs (maximized on binary masses, initial time and phase) between full NR (or hybrid waveforms, depending on the total binary mass) and several time and frequency domain PN template families. For time-domain PN templates and binary masses  $10M_\odot < M < 20M_\odot$ , for which the merger/ring-down phases do not contribute significantly to the total detector signal power, we confirm results obtained in Refs. [10, 11], notably that Tpn(3.5) and Epn(3.5) models have high FFs with good parameter estimation, i.e., they are faithful. We found that the frequency-domain SPA family has high FFs only for binary systems with  $M < 20M_\odot$ , for which most of the signal power comes from the early stages of inspiral. Furthermore, we found that it is possible to improve the SPA family by either extending it to unphysical regions of the parameter space (as done with BCV templates) or by introducing an *ad hoc* 4PN-order constant coefficient in the phase. Both modified SPA families achieve high FFs for high-mass binary systems with total masses  $30M_\odot < M < 120M_\odot$ .

For time-domain PN templates and binary masses  $M \gtrsim 30M_\odot$ , we found that if a superposition of ring-down modes is attached to the inspiral waveform, as naturally done in the EOB model, the FFs can increase from  $\sim 0.8$  to  $> 0.9$ . We tested the current Epn(3.5) template family obtained by attaching to the inspiral waveform three QNMs [10] around the EOB light-ring. In order to properly take into account the energy and angular-momentum released during the merger/ring-down phases we introduced [10] two physical parameters,  $\epsilon_M$  and  $\epsilon_J$ , whose dependence on the binary masses and spins will be determined by future comparisons between EOB and NR waveforms computed for different mass ratios and spins. We found high FFs  $\gtrsim 0.96$ . Due to small differences between EOB and NR waveforms during the fi-

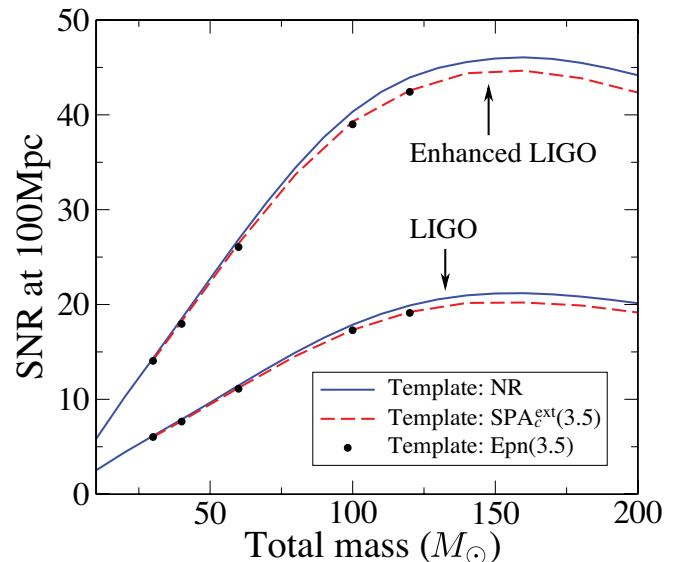


FIG. 16: The sky-average SNR for LIGO and Enhanced or mid LIGO detector versus total mass for an equal-mass binary at 100Mpc.

nal cycles of the evolution, the best-matches are reached at the cost of large systematic error in the merger–ring-down binary parameters. Thus, the Epn(3.5) template family can be used for detection, but for parameter estimation it needs to be improved when matching to the ring-down, and also during the inspiral phase. The refinements can be achieved (i) by introducing deviations from circular motion, (ii) adding higher-order PN terms in the EOB dynamics, (iii) using in the EOB radiation-reaction equations a GW energy flux closer to the NR flux, (iv) designing a better match to ring-down modes, etc.. The goal would be to achieve dephasing between EOB and NR waveforms of less than a few percent in the comparable-mass case, as obtained in Ref. [48] in the extreme mass-ratio limit. Indeed, with more accurate numerical simulations, especially those using spectral methods [49], it will be possible to *improve* the inspiraling templates by introducing higher-order PN terms in the analytic waveforms computed by direct comparison with NR waveforms.

Frequency-domain PN templates with an appropriate cutoff frequency  $f_{\text{cut}}$  provide high FFs ( $> 0.97$ ), even for large masses. This is due to oscillating tails (Gibbs phenomenon) produced when cutting the signal in the frequency domain. We tested the  $\text{SPA}_c^{\text{ext}}(3.5)$  and the  $\text{SPA}_c^{\text{y}}(4)$  template families for total masses up to  $120M_\odot$ , and three mass ratios  $m_2/m_1 = 1, 1.5$ , and  $2$ . We always get FFs  $> 0.96$ , even when using a fixed cutoff frequency,  $f_{\text{cut}} = 1.07\omega_{220}/2\pi$ . Because of its high efficiency, faithfulness, i.e., low systematic error in parameter estima-

tion, and simple implementation, the  $\text{SPA}_c^{\mathcal{Y}}(4)$  template family (or variants of it which include Lorentzians) is, together with the EOB model, a good candidate for searching coherently for GWs from binary systems with total masses up to  $120M_\odot$ .

In Fig. 16, we show the sky averaged SNRs of a single LIGO and Enhanced or mid LIGO [50] detector, for an equal-mass binary at 100Mpc. The SNR peaks at the total binary mass  $M \simeq 150M_\odot$  and shows the importance of pushing current searches for coalescing binary systems to  $M > 100M_\odot$ . In the mass range  $30M_\odot < M < 120M_\odot$ , the SNR drops only slightly if we filter the GW signal with  $\text{SPA}_c^{\text{ext}}(3.5)$  or  $\text{Epn}(3.5)$  instead of using NR waveforms. The difference between  $\text{Epn}(3.5)$  and  $\text{SPA}_c^{\text{ext}}(3.5)$  is almost indistinguishable. When  $M > 120M_\odot$ , although the  $\text{SPA}_c^{\text{ext}}(3.5)$  and  $\text{Epn}(3.5)$  template families give fairly good SNRs, it is maybe not a good choice to use them as the number of cycles reduces to a few. The key problem in detecting such GWs is how to veto triggers from non-Gaussian, nonstationary noise, instead of matching the effectively short signal. This is a general problem in searches for short signals in ground-based detectors.

### Acknowledgments

A.B. and Y.P. acknowledge support from NSF grant PHY-0603762, and A.B. also from the Alfred Sloan Foundation. The work at Goddard was supported in part by NASA grants O5-BEFS-05-0044 and 06-BEFS06-19. B.K. was supported by the NASA Postdoctoral Program at the Oak Ridge Associated Universities. S.T.M. was supported in part by the Leon A. Herreid Graduate Fellowship. Some of the comparisons with PN and EOB models were obtained building on Mathematica codes developed in Refs. [14, 30, 31, 45]

### APPENDIX A: COMMENT ON WAVEFORMS OBTAINED FROM THE ENERGY-BALANCE EQUATION

In adiabatic PN models, like the Tpn model used in this paper, waveforms are computed under the assumption

that the binary evolves through an adiabatic sequence of quasi-circular orbits. More specifically, one sets  $\dot{r} = 0$  and computes the orbital frequency  $\omega$  from the energy-balance equation  $dE(\omega)/dt = \mathcal{F}(\omega)$ , where  $E(\omega)$  is the total energy of the binary system and  $\mathcal{F}(\omega)$  is the GW energy flux. Both  $E(\omega)$  and  $\mathcal{F}(\omega)$  are computed for circular orbits and expressed as a Taylor expansion in  $\omega$ . The adiabatic evolution ends *in principle* at the innermost circular orbit (ICO) [35], or minimum energy circular orbit (MECO) [30], where  $(dE/d\omega) = 0$ .

By rewriting the energy-balance equation,  $\omega(t)$  can be integrated directly as

$$\dot{\omega}(t) = \frac{\mathcal{F}(\omega)}{dE(\omega)/d\omega}. \quad (\text{A1})$$

The RHS of Eq. (A1) can be expressed as an expansion in powers of  $\omega$ . The expanded version is widely used in generating adiabatic PN waveforms [20, 30, 31, 45], it is used to generate the so-called Tpn template family. It turns out that Tpn(3) and Tpn(3.5) are quite close to the NR inspiraling waveforms [10, 11]. We wonder whether using the energy-balance in the form of Eq. (A1), i.e., without expanding it, might give PN waveforms closer to or farther from NR waveforms. In principle the adiabatic sequence of circular orbits described by Eq. (A1) ends at the ICO, so the adiabatic model should work better until the ICO and start deviating (with  $\omega$  going to infinity) from the exact result beyond it.

In Fig. 17 we show the NR orbital frequency  $\omega(t)$  together with the PN orbital frequency obtained by solving the unexpanded and expanded form of the energy-balance equation. The frequency evolution in these two cases is rather different, with the orbital-frequency computed from the expanded energy-balance equation agreeing much better with the NR one. When many, extremely accurate, GW cycles from NR will be available, it will be worthwhile to check whether this result is still true.

- 
- [1] A. Abramovici et al., Science **256**, 325 (1992); <http://www.ligo.caltech.edu>.
  - [2] H. Lück et al., Class. Quant. Grav. **14**, 1471 (1997); <http://www.geo600.uni-hannover.de>.
  - [3] M. Ando et al., Phys. Rev. Lett. **86**, 3950 (2001); <http://tamago.mtk.nao.ac.jp>.
  - [4] B. Caron et al., Class. Quant. Grav. **14**, 1461 (1997); <http://www.virgo.infn.it>.
  - [5] [http://www.lisa-science.org/resources/talks-articles/science/lisa\\_science\\_case.pdf](http://www.lisa-science.org/resources/talks-articles/science/lisa_science_case.pdf)
  - [6] F. Pretorius, Phys. Rev. Lett. **95**, 121101 (2005).
  - [7] M. Campanelli, C.O. Lousto, P. Marronetti, and Y. Zlochower, Phys. Rev. Lett. **96**, 111101 (2006).
  - [8] J. Baker, J. Centrella, D. Choi, M. Koppitz, and J. van Meter, Phys. Rev. Lett. **96**, 111102 (2006).
  - [9] M. Campanelli, C.O. Lousto, and Y. Zlochower, Phys. Rev. D **74**, 041501 (2006); *ibid.* D **74**, 084023 (2006); U. Sperhake, `gr-qc/0606079`; J. González, U. Sperhake, B. Brügmann, M. Hannam, and S. Husa, Phys. Rev. Lett. **98**, 091101 (2007); B. Szilagyi, D. Pollney, L. Rezzolla,

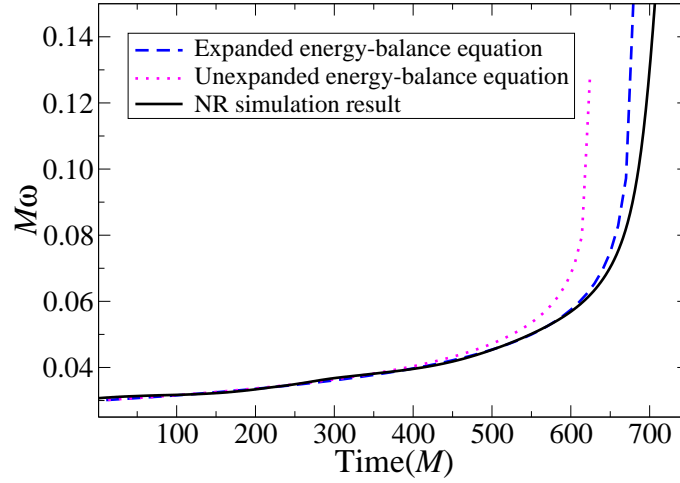


FIG. 17: Orbital frequency evolution. The dotted and dashed curves are calculated from the unexpanded and expanded energy-balance equations. The continuous curve refers to the really long Goddard NR simulation.

- J. Thornburg and J. Winicour, [gr-qc/0612150](#); F. Pretorius and D. Khurana, [gr-qc/0702084](#).
- [10] A. Buonanno, G. Cook, and F. Pretorius, *Phys. Rev. D* **75** (2007) 124018.
- [11] J. Baker, J. van Meter, S. McWilliams, J. Centrella, and B. Kelly (2006), [gr-qc/0612024](#).
- [12] P. Jaranowski, and G. Schäfer, *Phys. Rev. D* **57**, 7274 (1998); Erratum-ibid *D* **63** 029902; L. Blanchet, and G. Faye, *Phys. Rev. D* **63**, 062005 (2001); V. C. de Andrade, L. Blanchet, and G. Faye, *Class. Quant. Grav.* **18**, 753 (2001); T. Damour, P. Jaranowski, and G. Schäfer, *Phys. Lett. B* **513**, 147 (2001); L. Blanchet, G. Faye, B.R. Iyer, and B. Joguet, *Phys. Rev. D* **65**, 061501(R) (2002); L. Blanchet, and B.R. Iyer, *Class. Quant. Grav.* **20**, 755 (2003); Erratum-ibid *D* **71**, 129902 (2005); L. Blanchet, T. Damour, G. Esposito-Farese, and B.R. Iyer, *Phys. Rev. Lett.* **93**, 091101 (2004).
- [13] A. Buonanno, and T. Damour, *Phys. Rev. D* **59**, 084006 (1999).
- [14] A. Buonanno, and T. Damour, *Phys. Rev. D* **62**, 064015 (2000).
- [15] A. Buonanno, and T. Damour, *Proceedings of IX<sup>th</sup> Marcel Grossmann Meeting (Rome, July 2000)*, [gr-qc/0011052](#).
- [16] T. Damour, P. Jaranowski, and G. Schäfer, *Phys. Rev. D* **62**, 084011 (2000).
- [17] T. Damour, *Phys. Rev. D* **64**, 124013 (2001).
- [18] A. Buonanno, Y. Chen, and T. Damour, *Phys. Rev. D* **74**, 104005 (2006).
- [19] T. Damour, B.R. Iyer, and B.S. Sathyaprakash, *Phys. Rev. D* **57**, 885 (1998).
- [20] T. Damour, B. Iyer, and B. Sathyaprakash, *Phys. Rev. D* **63**, 044023 (2001); *ibid.* *D* **66**, 027502 (2002).
- [21] T. Baumgarte, P. Brady, J.D.E. Creighton, L. Lehner, F. Pretorius, and R. DeVoe (2006), [gr-qc/0612100](#).
- [22] J. W. York, Jr., *Phys. Rev. Lett.* **82**, 1350 (1999).
- [23] E. Gourgoulhon, P. Grandclément, and S. Bonazzola, *Phys. Rev. D* **65**, 044020 (2002).
- [24] P. Grandclément, E. Gourgoulhon, and S. Bonazzola, *Phys. Rev. D* **65**, 044021 (2002).
- [25] H. P. Pfeiffer L. E. Kidder, M. S. Scheel, and S. A. Teukolsky, *Comp. Phys. Comm.* **152**, 253 (2003).
- [26] G. B. Cook, and H. P. Pfeiffer, *Phys. Rev. D* **70**, 104016 (2004); M. Caudill, G.B. Cook, J.D. Grigsby, and H. Pfeiffer, *Phys. Rev. D* **74**, 064011 (2006).
- [27] S. Brandt and B. Brügmann, *Phys. Rev. Lett.* **78**, 3606 (1997).
- [28] C. Cutler et al., *Phys. Rev. Lett.* **70**, 2984 (1993).
- [29] T. Damour, B.R. Iyer, and B.S. Sathyaprakash, *Phys. Rev. D* **67**, 064028 (2003).
- [30] A. Buonanno, Y. Chen, and M. Vallisneri, *Phys. Rev. D* **67**, 104025 (2003); Erratum-ibid. *D* **74**, 029904 (2006).
- [31] A. Buonanno, Y. Chen, and M. Vallisneri, *Phys. Rev. D* **67**, 024016 (2003); Erratum-ibid. *D* **74**, 029903 (2006).
- [32] T. Damour, B. Iyer, P. Jaranowski, and B. Sathyaprakash, *Phys. Rev. D* **67**, 064028 (2003).
- [33] K. G. Arun, B.R. Iyer, B.S. Sathyaprakash, and P. Sundararajan, *Phys. Rev. D* **71**, 084008 (2005); Erratum-ibid *D* **72**, 069903 (2005).
- [34] T. Damour, E. Gourgoulhon, and P. Grandclément, *Phys. Rev. D* **66**, 024007 (2002); P. Grandclément, E. Gourgoulhon, and S. Bonazzola, *Phys. Rev. D* **65**, 044021 (2002).
- [35] L. Blanchet, *Phys. Rev. D* **65**, 124009 (2002).
- [36] L.S. Finn, *Phys. Rev. D* **46**, 5236 (1992); L. S. Finn and D.F. Chernoff, *Phys. Rev. D* **47**, 2198 (1993); É.E. Flanagan and S.A. Hughes, *Phys. Rev. D* **57**, 4535 (1998).
- [37] [http://www.ligo.caltech.edu/advLIGO/scripts/ref\\_des.shtml](http://www.ligo.caltech.edu/advLIGO/scripts/ref_des.shtml)
- [38] J. Baker, S. McWilliams, J. van Meter, J. Centrella, D. Choi, B. Kelly, and M. Koppitz (2006), [gr-qc/0612117](#).
- [39] J. Baker, M. Campanelli, F. Pretorius, and Y. Zlochower (2007), [gr-qc/0701016](#).
- [40] B. Abbott et al. (LIGO Scientific Collaboration), *Phys. Rev. D* **72**, 082001 (2005).
- [41] B. Abbott et al. (LIGO Scientific Collaboration), *Phys. Rev. D* **73**, 062001 (2006).
- [42] E. Berti, V. Cardoso, and C. Will, *Phys. Rev. D* **73**, 064030 (2006).
- [43] L. Blanchet, *Living Rev. Rel.* **9** (2006) 4.
- [44] T. Damour, B. Iyer, and B. Sathyaprakash, *Phys. Rev. D* **62**, 084036 (2000).

- [45] Y. Pan, A. Buonanno, Y. Chen, and M. Vallisneri, Phys. Rev. D **69**, 104017 (2004).
- [46] P. Ajith et al. (2007) (in preparation).
- [47] E. Berti, V. Cardoso, J. González, U. Sperhake, M. Hannam, S. Husa, and B. Brügmann (2007), [gr-qc/0703053](#).
- [48] A. Nagar, T. Damour, and A. Tartaglia, [gr-qc/0612096](#)
- T. Damour, and A. Nagar, Proceedings of XI<sup>th</sup> Marcel Grossmann Meeting (Berlin, July 2006), [gr-qc/0612151](#).
- [49] H. P. Pfeiffer, D.A. Brown, L.E. Kidder, L. Lindblom, G. Lovelace, and M. A. Scheel (2007), [gr-qc/0702106](#).
- [50] <http://www.ligo.caltech.edu/~rana/NoiseData/S6/DCnoise.txt>.